Applied Thermal Engineering

Experimental study of heat transfer characteristics of finned-tube and circular-pore heat exchangers in oscillatory flow

--Manuscript Draft--

Manuscript Number:	ATE-D-20-00722R2
Article Type:	Original Research Papers
Keywords:	Thermoacoustics; Heat Exchangers; heat transfer; Oscillatory flow
Corresponding Author:	Antonio Piccolo University of Messina ITALY
First Author:	Antonio Piccolo
Order of Authors:	Antonio Piccolo
	Artur Jaworski
Abstract:	This work is concerned with an experimental investigation of the thermal performance of two thermoacoustic heat exchangers characterized by different pore geometries, namely a circular-pore geometry and a finned-tube geometry. A standing wave engine, where the heat exchangers under test play the role of ambient HXs, is used as test-rig. Heat transfer rates measurements by standard energy balance techniques and dynamic pressure measurements are used to assess the impact of the two heat exchangers on the engine performance. The gas-side heat transfer coefficient, expressed as Nusselt number, is also determined for the finned-tube heat exchanger. The resulting values are compared to the heat transfer coefficients estimated in analogous experimental studies and by predictive models. Results show that the circular-pore heat exchanger reduces the performance of the engine compared to the finned-tube heat exchanger by about 23%, being affected by higher thermal and viscous irreversibility. Moreover, the boundary layer conduction model exhibits a better agreement with the measured heat transfer coefficients compared to other models. A new correlation law, based on regression of the experimental data, is also derived.
Suggested Reviewers:	William Zimmerman w.zimmerman@sheffield.ac.uk He has expertise in thermoacoustic systems
	Andrew Nowakowski a.f.nowakowski@sheffield.ac.uk He has expertise in thermoacoustic systems
	Hussam Jouhara hussam.jouhara@brunel.ac.uk He has expertise in thermoacoustic systems
	Tetsushi Biwa biwa@m.tohoku.ac.jp He has expertise in thermoacoustic systems
Response to Reviewers:	

Powered by Editorial Manager® and ProduXion Manager® from Aries Systems Corporation

Experimental study of heat transfer characteristics of finned-tube and circular-pore heat exchangers in oscillatory flow

Antonio Piccolo[a](*), Artur J. Jaworski[b]

[a]*Department of Engineering, University of Messina, Contrada di Dio, 98166 S. Agata (Messina) Italy*
[b]*School of Computing and Engineering, University of Huddersfield, Huddersfield, HD1 3DH, UK*

Abstract. This work is concerned with an experimental investigation of the thermal performance of two thermoacoustic heat exchangers characterized by different pore geometries, namely a circular-pore geometry and a finned-tube geometry. A standing wave engine, where the heat exchangers under test play the role of ambient HXs, is used as test-rig. Heat transfer rates measurements by standard energy balance techniques and dynamic pressure measurements are used to assess the impact of the two heat exchangers on the engine performance. The gas-side heat transfer coefficient, expressed as Nusselt number, is also determined for the finned-tube heat exchanger. The resulting values are compared to the heat transfer coefficients estimated in analogous experimental studies and by predictive models. Results show that the circular-pore heat exchanger reduces the performance of the engine compared to the finned-tube heat exchanger by about 23%, being affected by higher thermal and viscous irreversibility. Moreover, the boundary layer conduction model exhibits a better agreement with the measured heat transfer coefficients compared to other models. A new correlation law, based on regression of the experimental data, is also derived.

Keywords: Thermoacoustics; Heat exchangers; Heat transfer; Oscillatory flow

(*) **Corresponding author. Tel**.: +39 090 6765311, **email**: apiccolo@unime.it

Highlights

- The thermal performance of finned-tube and circular-pore heat exchangers is studied.
- The effect of pore geometry and porosity on engine performance is assessed.
- Finned-tube heat exchanger improves engine performance due to lower irreversibility.
- The dimensionless heat transfer coefficient vs acoustic Reynolds number is derived.
- The Boundary Layer Conduction model has the best agreement with experimental data.

Nomenclature

A	total cross section area, m^2
A_f	fin cross section area, m^2
A_g	cross section area open to gas flow, m^2
AHX	ambient heat exchanger
A_1, A_2	empirically fitted parameters
c_w	water specific heat, J/kgK
d	tube wall thickness, m
D_h	hydraulic diameter, m
DR	drive ratio (P_A/P_m)
f	frequency, Hz
g	HX-stack separation gap, m
h	gas-side heat transfer coefficient, W/m^{2}K
h_w	water-side heat transfer coefficient, W/m^{2}K
K	gas thermal conductivity, W/mK
K_f	fin thermal conductivity, W/mK
K_t	tube thermal conductivity, W/mK
L	plate length, m
L_f	half fin length, m
L_{HX}	heat exchanger length, m
L_T	thermal entry length, m
m	fin parameter
Nu	Nusselt number
p	acoustic pressure (Pa)
P_A	pressure amplitude at a pressure antinode, Pa
P_m	mean pressure, Pa
Pr	Prandtl number
P1,..,P3	pressure sensors
$\dot{Q}$	convective heat transfer rate, W
$\dot{Q}_A$	AHX heat transfer rate, W
$\dot{Q}_H$	input heat transfer rate, W
$\dot{Q}_{K1}$,$\cdot\dot{Q}_{K3}$	conductive heat transfer rate, W
$\dot{Q}_{leak}$	leakage heat transfer rate, W
Re	acoustic Reynolds number
R_h	hydraulic radius, m
T1,..,T6	temperature sensors
U	volumetric velocity, m^3/s
UA	overall heat transfer coefficient, W/K
$\dot{V}$	water volume flow rate, m^3/s
Va	Valensi number
v_1	local velocity amplitude, m/s
W_a	acoustic power, W
x	axial irection, m
x_{eff}	min{$2\xi_1$, L_{HX}}
y_{eff}	min{R_h, δ_κ}

Greek symbols

Δ	difference
ΔT_{ms}	gas-solid temperature difference, K
δ_κ	thermal penetration depth, m
η	engine efficiency
η_C	Carnot’s efficiency
η_f	fin efficiency
θ_{ml}	log-mean temperature difference, K
κ	gas thermal diffusivity, m^2 s^{-1}
μ	dynamic viscosity, Ns/m^2
ξ_1	displacement amplitude, m
Π	fin cross-section perimeter, m
ρ_m	gas density, kg/m^3
ρ_w	water density, kg/m^3
ϕ	porosity
ω	angular frequency, rad/s

Subscripts

A	ambient, peak amplitude
D	diameter
f	fin
g	gas
H	hot, heater

S	gas-solid heat transfer area, m^2	HX	heat exchanger
S_b	unfinned surface area, m^2	L	length
S_w	inner tube surface, m^2	m	mean
t	fin thickness, m	RMS	Root Mean Square Reynolds Number
T_H	heater temperature, K	$static$	static measurement
T_m	local gas temperature, K	$TASFE$	Time-Average Steady-Flow Equivalent
T_s	temperature at the fin base, K	w	water
T_1, T_2	inlet/outlet water temperature, K	1	first-order acoustic variable
T_2'	corrected outlet temperature of water, K		

1. Introduction.

In thermoacoustic (TA) engines the heat exchanger (HX) plays the fundamental role of providing the heat transfer between external thermal reservoirs and the core of the engine, namely a porous media of high thermal capacity (stack/regenerator) where the heat/sound energy conversion takes place. Although the theoretical foundations of TA energy conversion were formulated by Rott in the seventies of last century [1] the design methodologies of this component are not yet well-established.

The main issues involved in its design arise from it working under oscillatory flows with short acoustic displacement. This fact has two important implications: (a) the heat transfer area cannot be increased by simply increasing the HX length along the direction of the acoustic oscillation; (b) standard steady flow correlations for compact HXs cannot be directly applied. The first point demands for clear rules on selection of the optimal geometrical configuration of the HX (length, pore hydraulic radius etc.) for a given application. The last point demands for reliable heat transfer correlations specific to oscillatory flows in the dynamic range typical of TA engines. Both theoretical and experimental approaches were applied to investigate the above issues.

As for the first issue, the basic design rule of TA HXs was first given by Swift [2] who argued that the length of the HXs (L_{HX}) along the direction of acoustic oscillation (*x*-direction thereafter) should be of the order of (and not exceed) the peak-to-peak displacement amplitude ($2\xi_1$). In a later research Swift [3] found experimental evidence of improvement in engines' performance for HXs of reduced length ($\sim\xi_1$). It is also suggested that the hydraulic radius of the HX pores, R_h, should be of the order of the thermal penetration depth (δ_κ), which represents the distance over which heat diffuses in an acoustic cycle. This statement derives from considering that the gas responsible for heat transport to/from the stack oscillates at a distance δ_κ from the gas-solid boundary. Analogously, Minner et al. [4] found, on the basis of an optimization study of TA refrigerators, that the optimal value of the normalized distance R_h/δ_κ should range from 2 to 4.

Cao et al. [5] evidenced, through numerical simulation of parallel-plate stacks, that the lengths L_{HX} and R_h are correlated: the smaller the pore hydraulic radius the shorter the HX length. This result, also found in other computational investigations [6-7], indicates that the length of HXs with small pores ($R_h/\delta_\kappa<1$) could be shorter than $2\xi_1$ and about equal to the particle displacement distance (ξ_1). Even lower values ($L_{HX}/\xi_1 \sim 0.6$) were found by Besnoin and Knio [8] although the same authors found lengths exceeding $2\xi_1$ in a subsequent study [9].

Entropy generation minimization methods [10-12] showed that the above correlation should result as a trade-off between the thermal irreversibility associated with heat transfer and the irreversibility associated with viscous and thermal dissipation. This trade-off, producing a minimum in entropy generation, happens at lower L_{HX} values as R_h is reduced due to quadratic increase of the viscous dissipation with R_h for $R_h \to 0$.

The numerical studies of Besnoin and Knio [8, 9] and Marx and Blanc-Benon [13] evidenced that, in addition to L_{HX} and R_h, the separation gap *g* between a stack and the adjacent HX could have a considerable influence on the HX performance. In a real TA device this gap minimizes adverse thermal conduction from the hot to the cold HX and prevents the HX to obstruct the regenerator/stack pores. The optimal gaps found in these studies at the investigated configurations lie in the range 0.12–0.2 ξ_1.

The effect of difference in porosity ϕ (defined as the ratio of cross-section area open to gas flow, A_g, to total area, A) between the HX and adjacent stack is considered [4] to be responsible of complex turbulent flow patterns which actually increase the friction losses at the junction [3]. To avoid these adverse entrance problems Tijani et al. [14] suggested that the porosity of the HX should match the porosity of the stack. This recommendation, formulated for standing wave devices, could not be fully applicable to travelling wave devices where the HX porosity is in some cases set to produce deliberate phase shifting of the acoustic wave [15].

Optimal design of TA HXs entails therefore setting proper values of the four geometrical parameters L_{HX}, R_h, g, ϕ, but clear and univocal guidelines establishing how these parameters must be related in an optimized configuration have not been to date formulated.

As for the second issue, the calculation of the gas-side heat transfer coefficient h relies principally on the model formulated by Swift [3], the so called "Boundary Layer Conduction" (BLC) model (also integrated in the design code "DeltaEC" [16]). This model states $h=K/y_{eff}$ where K is the gas thermal conductivity and y_{eff} is the minimum between R_h and δ_κ.

Other relevant models are the "Time-Average Steady-Flow Equivalent" (TASFE) [17] and the "Root Mean Square Reynolds Number" (RMS-Re) [18] models which similarly try to derive non-dimensional heat transfer correlations for the TA case by time averaging over an acoustic cycle classical steady-flow correlations.

A number of experimental investigations, involving different HX geometries and test conditions, were carried out to validate the above models and to define robust correlations for the estimation of h in oscillatory flows [19-24]. The results reported in these studies indicate that the application of the TASFE and RMS-Re models may introduce significant errors in predicting the h value. Furthermore, the experimentally derived correlations are ambiguous and configuration dependent.

The above discussion show how current knowledge on the design of efficient HXs for TA applications is not yet exhaustive. As a result, additional research is needed to investigate on the impact of HX geometry on heat transfer and to develop reliable correlations for the determination of the gas-side heat transfer coefficient under oscillatory flow conditions.

With this purpose in this paper the results of an experimental research aimed at studying the impact of two HXs characterized by a different geometry (circular and finned) on the global thermoacoustic system performance and at deriving (in the finned geometry case) proper heat transfer correlations are presented. The test-rig is a TA engine of the standing-wave type where the investigated HXs play the role of ambient HXs. Engine performance and HXs heat transfer rates are determined over a wide range of velocity amplitudes through standard sound pressure and energy balance measurements. The derived correlation law, expressed in terms of Nusselt number, is then compared to analogous measurements found in literature and to the predictions of the models discussed above.

2. Experimental setup and data reduction.

2.1 Experimental apparatus

The test-rig considered for this research consists of a standing wave thermoacoustic engine using air at atmospheric pressure as working fluid. It is characterized by a resonance frequency of 143.2

Hz and by an onset temperature difference of about 350 °C. A schematic of the engine is shown in Fig. 1.

The resonator is made of stainless steel and comprises a “hot” duct with a diameter of 10.5 and 10 cm long, a “stack holder” with a diameter of 10.5 cm and 8 cm long, a conical shaped segment (taper angle ~15°), a narrow duct with a diameter of 5.3 cm and 20 cm long and a buffer volume (a closed conical shaped duct with taper angle ~15°).

The stack is a ceramic (cordierite) honeycomb stack 7.9 cm long in the *x* direction. The pores have a squared shape with R_h=0.28 mm while the cell density is near 400 cpsi.

The electric heater is fabricated by wrapping about 3.7 m of a Ni-Cr wire (12 Ω/m) uniformly in and out the pores of a honeycomb ceramic slice 1 cm long in the *x* direction (and made of the same material of the stack) that served as a support. A 2 cm long stainless-steel ring equipped with feedthroughs for power cables is used to accommodate the slice.

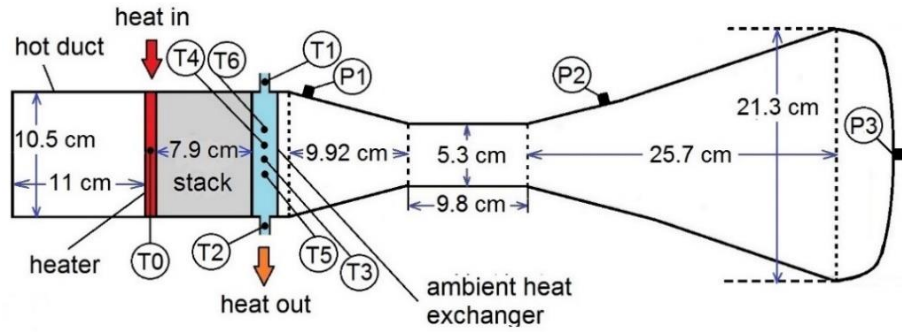

Figure 1. Schematic of the standing wave test engine. Labels “T” indicate thermocouple location. Labels “P” indicate microphone location.

The HXs under test are two cross-flow HXs with four water-tube passes. A picture of the two HXs, which in the engine arrangement work as ambient HXs, is shown in Fig. 2.

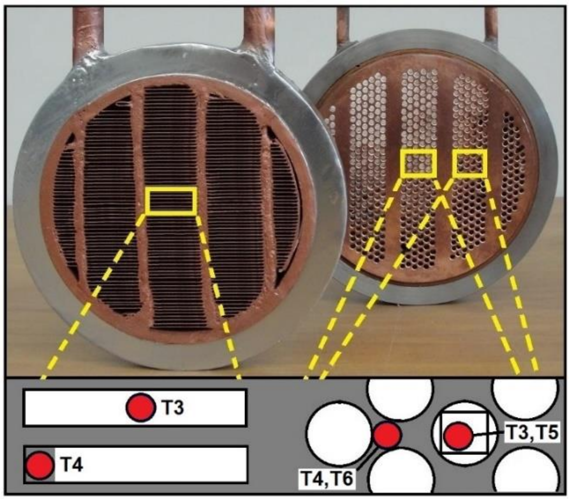

Figure 2. The heat exchanger with finned-tube (on the left) and circular-pore (on the right) geometry. Red circles indicate thermocouples.

The first HX (AHX1) is of the finned-tube type. It is 2 cm long in the *x* direction. For its fabrication a copper ring 2 cm thick with an internal radius of 10.5 cm and an external radius of

14 cm was used as mechanical support of the HX itself. Just outside the HX the cooling water flows through a copper tube with a diameter of 14 mm which has been crushed to obtain a rectangular cross section pipe of area 2 cm×0.5 cm. The crushed pipe has then been bent six times to allow for four passages in the front section of the HX as shown in Fig. 2. The fins are made of strips of laminated copper 0.45 mm thick and 2 cm wide. These strips have been welded to the external walls of the pipe with a fin spacing of 1.1 mm (resulting in R_h=0.55 mm). The porosity of this HX (ϕ_1) is calculated to be around 54%.

The second ambient heat exchanger (AXH2) is fabricated from a circular copper block and is 2 cm long in the *x* direction. Gas passages are obtained by drilling 574 holes with a diameter of 2.5 mm in parallel to its axis. Cooling water passages are obtained by drilling 4 channels with a diameter of 5 mm perpendicularly to the HX axis. The water also flows partially around the perimeter of the block. The porosity of this HX (ϕ_2) is about 33%. The hydraulic radius of the pores is R_h≈0.6 mm. Compared to AHX1 this HX is characterized by a simpler fabrication technique but the circular pore geometry hardly allows for porosities to exceed 40 %.

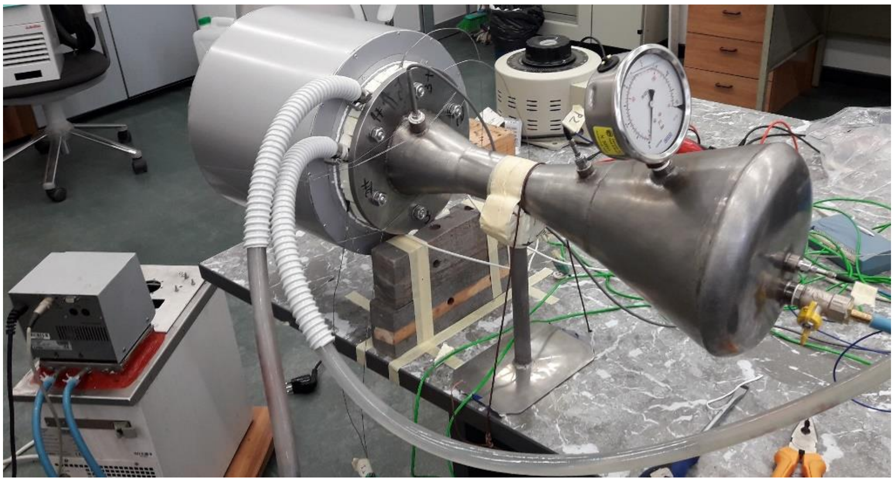

Figure 3. Photograph of the experimental apparatus.

Note that these two HXs are both made of copper, have the same length along the resonator axis (2 cm), have pores of almost equal hydraulic radius and have the same flow arrangement (cross flow with four water-tube passes). Their comparative study should therefore allow for investigating the impact of pore geometry and associated porosity on the engine performance.

At the working frequency of the engine (f≈143 Hz) the thermal penetration depth of the gas

$$\delta_\kappa = \sqrt{\frac{2\kappa}{\omega}} \qquad (1)$$

(κ and ω being the gas thermal diffusivity and the angular frequency respectively) amounts approximately to δ_κ≈0.23 mm so that R_h/δ_κ≈2.2 for AHX1 and R_h/δ_κ≈2.6 for AHX2. These values are compatible with good thermal contact conditions between the gas and the HX solid walls [4]. Spacers were used to separate the HXs from the stack by a gap of about 1.5 mm.

The standing wave engine in place for testing is shown in Fig. 3. The cylindrical sleeve seen on the left is filled with rock wool to thermally insulate the “hot” parts of the engine (the hot duct, the heater and the stack holder). A strip of a polystyrene sheet 2 cm thick has been also wrapped around the ambient HXs for thermal insulation purposes.

2.2 Measurements

For dynamic pressure measurements a microphone (Brüel and Kjær instruments, type 4938, sensitivity 1.6 mV/Pa) and two piezoelectric pressure transducers (PCB Piezotronics, model 113B28, sensitivity 14.5 mV/kPa) were flush mounted on the resonator walls. The signals recorded by these sensors (labeled as P1, P2 and P3 in Fig. 1), when combined with simulations performed using the DeltaEC code (configured for matching the P1, P2 and P3 values) make it possible to reconstruct the profile of the acoustic wave along the resonator axis and to estimate parameters of interest such as the amplitude of the dynamic pressure at a pressure antinode (P_A), the amplitude of the oscillatory velocity at the HXs location (v_1) and the flow of acoustic energy across a given section or component. A typical result is shown in Fig. 4 where the axial distributions of the magnitude of the acoustic pressure, p, and volumetric velocity, U, are reported. It can be seen how the AHX is located around midway between the velocity node and antinode of the standing wave so that a wide range of velocity amplitudes (and associated gas displacement amplitudes) can be selected by varying the heat input to the system.

To measure the average gas/solid temperature of the heater, T_H, a type-K thermocouple (error ±0.3 °C), labeled as T0 in Fig. 1, was placed inside a pore located at the centre of the heater.

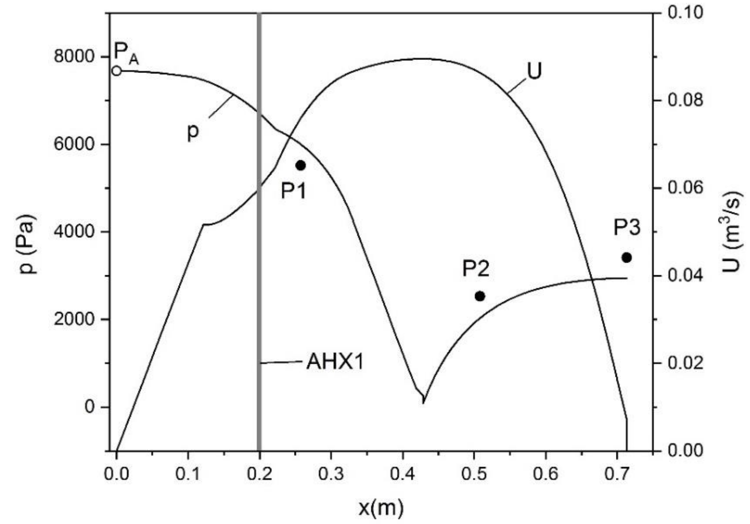

Figure 4. Axial distributions of the magnitude of the acoustic pressure, p, and volumetric velocity, U, when the heat input to the engine (integrating AHX1) is 583 W. Full circles are the pressure values measured by P1, P2 and P3. The vertical grey line indicates the AHX location.

As for AHX1, two type-K thermocouples (labeled as T1 and T2) were placed in the water tubing at the inlet and outlet sections of the HX to measure the local water temperature (T_1 and T_2 respectively). To measure the temperature T_m of the gas flowing inside a pore a thermocouple (labeled as T3) was installed through a spacer in the (slightly enlarged) gap between two fins located at the centre of the HX. To measure the temperature T_s at the base of the fins a thermocouple (labeled as T4) was glued on the flat wall of the water pipe by copper spray. A schematic of the installation of T3 and T4 can be seen in Fig.2.

As for AHX2, two type-K thermocouples (labeled as T1 and T2) were placed in the water tubing at the inlet and outlet sections of the HX to measure the local water temperature (T_1 and T_2, respectively). To measure the temperature T_m of the gas flowing inside a pore a thermocouple (labeled as T3) was inserted into a ceramic sleeve of squared cross section and the assembly was then fitted in a (slightly enlarged) pore. Since the contact area between the sleeve and the pore walls is restricted to the sleeve corners this probe reasonably measured the temperature of the gas. To measure the temperature T_s of the solid honeycomb matrix a thermocouple (labeled as T4) was imbedded in a hole drilled in the copper matrix just near T3. Copper spry was used to enhance thermal contact. The remaining two thermocouples (labeled as T5 and T6) have been analogously installed to measure T_m and T_s but in a more peripherical location compared to T3 and T4 so as to get the information on the radial distribution of the measured temperatures. A schematic of the installation of T3, T4, T5 and T6 can be seen in Fig.2.

The thermocouple signals are acquired by a 8-channel data logger connected to a PC (USB-Temp device of Measurement Computing) while the dynamic pressure sensor signals are read, after being preamplified, directly on multimeters as output voltages.

The input heat flux $\dot{Q}_H$, generated by feeding the heater through a variable voltage autotransformer, was calculated by measuring the voltage drop across the heater and the flowing current.

The heat power transferred by the AHX is measured through a closed loop water circuit. The network comprises (a) a refrigerated/heating circulator unit pumping the water and controlling its temperature, (b) a valve installed downstream the AHX regulating the water flow rate, (c) a rotameter (accuracy ± 5 l/h) installed upstream the AHX measuring the water flow rate and (d) a thermal storage system placed outdoors constituted by a copper coil immersed in a water bath. The last system was utilized because the circulator is unable to absorb thermal loads on the AHX higher than 200 W. The inlet temperature of the water is set at 25 °C in all measurements.

To avoid moisture condensation on the solid surfaces of the HXs and stack each measurement cycle started by emptying the resonator through a vacuum pump. While the vacuum pump is left in operation for at least ½ hour the heater is heated up to about 50÷60 °C and cooling water at 25 °C is sent into the AHX. Then the vacuum pump is disconnected and external air is left to enter the resonator. Finally, the engine is brought to the desired operating point and measurement is conducted after thermal equilibrium conditions are reached.

2.3 *Data reduction*

The AHXs' heat transfer rates are estimated from the measured inlet/outlet water temperatures and water volume flow rate, $\dot{V}$, as

$$\dot{Q}_A = \dot{V}\rho_w c_w (T_2 - T_1) \tag{2}$$

ρ_w and c_w being the density and specific heat of water respectively.

It must be observed that the measured heat flux $\dot{Q}_A$ comprises different contributions and precisely: (1) the thermo-acoustically activated hydrodynamic heat flux $\dot{Q}$ along the stack (the parameter of interest for the estimation of the gas-side heat transfer coefficient), (2) the conduction heat flux $\dot{Q}_{K1}$ transported by the gas and the solid portion of the stack, (3) the conduction heat flux $\dot{Q}_{K2}$ transported by the stack-holder walls and thermal insulating sleeve (4) the conduction heat flux $\dot{Q}_{K3}$ transported by the resonator walls over which dissipation of acoustic power occurs and finally (5) the conduction heat flux $\dot{Q}_{leak}$ due to heat leakage from the heat exchanger to the surrounding environment through the insulation. Heat balance provides the following equation

$$\dot{Q}_A = \dot{Q} + (\dot{Q}_{K1} + \dot{Q}_{K2} + \dot{Q}_{K3}) - \dot{Q}_{leak} \tag{3}$$

Therefore, to calculate $\dot{Q}$ the above conduction heat fluxes have to be estimated. To accomplish this a combination of both static measurements and simulation procedures is applied.

In the static measurements the heater was powered below the onset temperature of the engine and the thermal load on the AHX corresponding to

$$\dot{Q}_{A,static} = \dot{Q}_{K1} + \dot{Q}_{K2} - \dot{Q}_{leak} \tag{4}$$

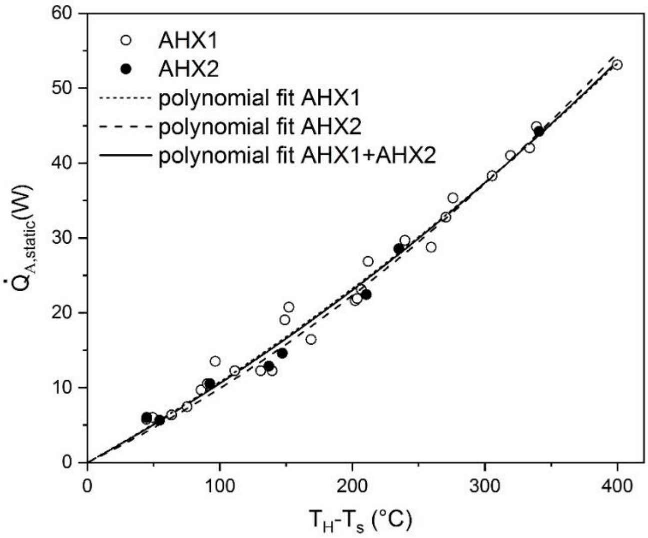

Figure 5. The conductive heat flux measured under static measurements for AHX1 (open circles) and AHX2 (full circles). Dotted, dashed and continuous lines are 2nd order polynomial fits of the experimental points concerning AHX1, AHX2 and both AHX1 and AHX2 respectively.

was measured through Eq. (2). Results are shown in Fig. 5 where $\dot{Q}_{A,static}$ is reported as a function of the temperature difference between the heater, T_H, and the AHX, T_s, for both AHX1 (open circles) and AHX2 (full circles). The least-squares fit of the two sets of experimental data by a 2nd order polynomial of the form $A_1(T_H\text{-}T_s)+A_2(T_H\text{-}T_s)^2$ is represented by the dotted (AHX1) and dashes (AHX2) lines. The relative difference between these two curves results lower than 5% according to the fact that the thermal path from the heater to the AHXs is equal in the two cases. So, for subsequent analysis the curve fit of all the experimental points (both AHX1 and AHX2) is considered. The resulting values for the fitting parameters are A_1=0.09624±0.00441 and A_2=(9.43334±1.54)×10^{-5}, the coefficient of determination being R^2=0.988. Subtracting now Eq. (4) from Eq. (3) provides

$$\dot{Q} = \dot{Q}_A - \dot{Q}_{A,static} - \dot{Q}_{K3} \tag{5}$$

The heat flux $\dot{Q}_{K3}$ to be substituted in this equation together with $\dot{Q}_{A,static}$ for the determination of $\dot{Q}$ was derived by simulating the energy fluxes in the engine using DeltaEC. The acoustic power flowing downstream the AHX toward the conical duct (on the right of the AHX in Fig. 1) is identified with $\dot{Q}_{K3}$.

Note that the above method does not require the direct determination of $\dot{Q}_{leak}$ since this term is included both in $\dot{Q}_{A}$ and in $\dot{Q}_{A,static}$ and it elides after Eq. (4) is subtracted from Eq. (3).

To make $\dot{Q}$ consistent with the outlet temperatures of water these last are recalculated as follows

$$T_2' = T_2 - \frac{(\dot{Q}_{A,static} + \dot{Q}_{K3})}{\rho_w c_w \dot{V}} \tag{6}$$

where T_2' represents the outlet temperature of water that would be measured if the conduction contributions were absent, i.e., if the AHX was uniquely loaded by the hydrodynamic heat flux.

The heat transfer and temperature values so determined are then used to calculate the overall heat transfer coefficient, *UA*, as [25]

$$UA = \frac{\dot{Q}}{\theta_{ml}} \tag{7}$$

where θ_{ml}, the log-mean temperature difference, has the following expression

$$\theta_{ml} = \frac{T_2' - T_1}{\ln\left(\dfrac{T_m - T_1}{T_m - T_2'}\right)} \tag{8}$$

when considering that in oscillatory flows the inlet and outlet temperatures of the primary fluid (the gas) are the same (T_m).

In the case of AHX1 the finned geometry allows the gas-side heat transfer coefficient *h* to be estimated from the *UA* values. A simplified 1D heat transfer model provides, in fact, the following expression for *UA*

$$UA = \frac{1}{\dfrac{1}{h_w S_w} + \dfrac{d}{K_t S_w} + \dfrac{1}{h\left[\sum_i (\Pi L_{fi})\eta_{fi} + S_b\right]}} \tag{9}$$

where h_w is the water-side heat transfer coefficient, S_w is the total inner surface of the water tubes, K_t is the thermal conductivity of the tube material (copper), *d* is the wall thickness of the tube, Π is the perimeter of the fin cross section, L_{fi} is half the length of the i-th fin, S_b is the total area of the unfinned external surface of the tubes and where η_{fi}, the efficiency of the i-th fin, has the following expression

$$\eta_{fi} = \frac{\tanh(mL_{fi})}{mL_{fi}} \qquad m = \sqrt{\frac{h\Pi}{A_f K_f}} \tag{10}$$

A_f and K_f being the cross-section area and thermal conductivity of the fin respectively.

In Eq. (9) the parameter h_w has to be measured beforehand. To accomplish this the AHX was set in isothermal conditions by immersing it in a water bath maintained at 50 °C. A flow $\dot{V}$ of water at 25 °C was then sent to the HX inlet section. If the temperature of the fin base T_s is assumed equal to the temperature of the internal surfaces of the water tube, standard energy balance calculations for the case of internal flow with constant surface temperature [25] provide the following expression of h_w in terms of measured quantities

$$h_w = \frac{\dot{V}\rho_w c_w}{S_w} \ln\left(\frac{T_s - T_1}{T_s - T_2}\right) \tag{11}$$

Obviously, the effectiveness of this procedure relies on the assumption of constant surface temperature that constitutes the major approximation of the method. However, using a thin tube wall (d=1 mm) and of high thermal conductivity (K_t≈400 W/mK) the approximation should be reasonable. For a water flow rate of 60 l/h, for example, the method furnished the value h_w=2496±21 W/m^{2}K (the indicated accuracy being the standard deviation of measurements).

2.4 Error analysis

To estimate the measurement uncertainty standard error propagation procedures [17] are applied. To reduce the error in the measurement of temperature differences ΔT an accurate in situ calibration of the thermocouples was performed by an environmental test chamber. This decreased the error in ΔT to ±0.2 °C. Analogously, the uncertainty in the measurement of the flow rate of water was decreased to ± 0.3 l/h after calibration of the rotameter through accurate measurements of the volume of water collected in a precision graduated cylinder in a given time. To reduce the error in the calculation of $\dot{Q}_A$ and θ_{ml} the flow rate of water was decreased gradually from 53.8 l/h at the highest heat transfer rates to 17.3 l/h at the lowest ones. This allowed for relatively large water temperature drop across the AHX (> 7 °C) maintaining, accordingly, the relative uncertainty on $\dot{Q}_A$ lower than 4.2% and that on θ_{ml} lower than 7 %. A higher relative error (~10 %) affects the measurement of the heat flux $\dot{Q}_{A.static}$ since the low conductive heat transfer rates give rise to smaller temperature differences across the AHXs (< 2.2 °C). From the above values it results that the relative error of the heat fluxes $\dot{Q}$ as calculated by Eq. (5) varies from about 4% at the highest heat transfer rates to 17 % at the lowest ones. Analogously, the relative error affecting the heat transfer coefficient h varies from about 8% to 24 %. These trends reflect the decrease in temperature differences across the AHX as the heat transfer rates are reduced. The uncertainty values of the Nusselt number are represented by error bars in Fig. 10.

3. Results and discussion

3.1 Impact of HXs on engine performance

The impact of the two HXs on the engine performance in converting heat to acoustic power can be deduced from Fig. 6 where the square of acoustic pressure amplitude measured by P1, P2 and P3 is reported as a function of the electric power input to the engine $\dot{Q}_H$ when a steady state is reached. Results show how AHX1 increases the engine performance compared to AHX2 since the acoustic pressure amplitudes measured at the selected microphone locations are higher for AHX1 than for AHX2 at every input power level.

The difference in performance cannot be fully captured from Fig 6, however, since the temperature difference across the stack, which influences the generated acoustic power, is different in the two cases as shown in Fig. 7 where (T_H-T_s) is reported as a function of $\dot{Q}_H$.

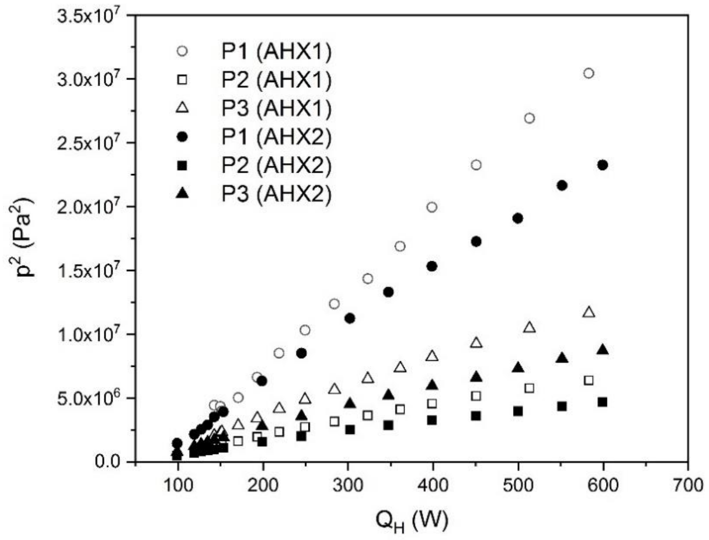

Figure 6. The square of the acoustic pressure measured by P1, P2 and P3 as a function of the heat input to the system.

So, for assessing the impact of the two HXs on the engine performance the thermal-to-acoustic conversion efficiency normalized by the Carnot efficiency is considered as a relevant indicator:

$$\frac{\eta}{\eta_C}=\frac{W_a}{\dot{Q}_H}\left(1-\frac{T_s}{T_h}\right)^{-1} \tag{12}$$

where W_a, the acoustic power produced by the engine core (the stack/HXs assembly), is calculated by DeltaEC (configured for matching the P1, P2 and P3 values) as the sum of the acoustic energy fluxes leaving the ambient HX and the heater from the sides facing the resonator. Results are shown in Fig. 7 where η/η_C is reported as a function of $\dot{Q}_H$. The normalized efficiency of the engine integrating AHX1 is reduced on average by 27% (the efficiency by 23%) when AHX2 is installed, despite the fact that in the last case a higher temperature gradient exists in the stack.

The lower performance of AHX2 and the higher operating temperature, seems to indicate that some acoustic loss mechanisms is at play that is more pronounced in AHX2 than AHX1. Furthermore, this loss mechanism grows with the acoustic amplitude since the difference between the temperature gradients of the two HXs increases with $\dot{Q}_H$.

Although AHX2 has a smaller heat transfer area compared to AHX1 the viscous dissipation occurring on the HXs surfaces could be, at least partially, responsible of the observed behavior. For a given volumetric flow, in fact, the local velocity amplitude v_1 in AHX2 should be about $\phi_1/\phi_2 \approx 1.64$ times higher than the velocity amplitude in AHX1. So, the viscous dissipation per unit area of AHX2 should be around $(\phi_1/\phi_2)^2 \approx 3.28$ times higher than the one on AHX1. Taking into account that AHX2 has surface area $\phi_2 R_{h1}/\phi_1 R_{h2} \approx 0.61$ times smaller than AHX1 it follows that the dissipation of acoustic power on AHX2 is almost double that on AHX1.

An additional loss mechanism could be caused by the complex flow structures occurring at the HX-stack and HX-duct junctions due to the difference in porosity. The fluid motion entering and leaving the HX pores is characterized, in fact, by turbulent flow through sharp corners during fluid entrance into the pores and vortex formation and shedding during the fluid ejection from the pores [26]. These effects are likely to be less important for AHX1 whose finned geometry and higher ϕ should minimize eddy production in the acoustic flow [27]. The dissipated power, assumed of the order of $A_g\rho_m v_1^3$ [18] (where ρ_m is the mean gas density) should be around 3 times higher in AHX2 than in AHX1.

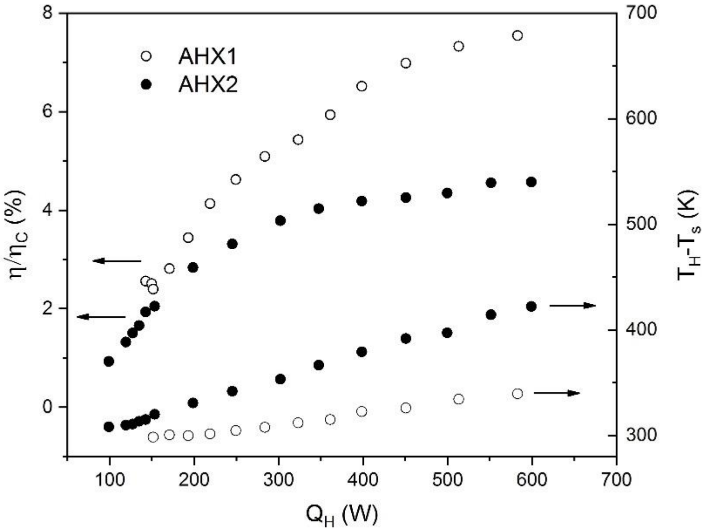

Figure 7. The normalized efficiency (on the left scale) and the temperature difference between the "hot" and "ambient" heat exchanger (on the right scale) as a function of the heat input to the system.

Although the above arguments could not fully account for the excess of the temperature difference (T_H-T_s) measured in AHX2 compared to AHX1 they illustrate that the HX pore geometry and porosity could have a non-trivial effect on flow losses, especially when the HX is located in high velocity regions of the acoustic field, as in the present investigation.

An additional explanation of the improved performance of the engine containing AHX1 is found when taking into account that a figure of merit of a HX reflects its ability to sustain high transfer rates under small gas-solid temperature differences. This favorable property, in fact, decreases the thermal irreversibility associated with the heat transfer and leads to an enhancement of the overall engine performance. The time averaged gas-solid temperature differences ΔT_{ms} ($=T_m$-T_s) measured for the two HXs are reported in Fig. 8 as a function of the drive ratio DR defined as the ratio of the pressure amplitude at the wave pressure antinode P_A (calculated by DeltaEC when configured for matching the P1, P2 and P3 values) to the mean pressure P_m.

As expected, AHX1 entails lower ΔT_{ms} values as being characterized by a lower UA factor. The last parameter, calculated by Eq. (7) for both HXs, is plotted in Fig. 9 as a function of the local peak acoustic Reynolds number

$$\mathrm{Re}_{D1} = \frac{\rho_m D_h v_1}{\mu} \tag{13}$$

where D_h is the hydraulic diameter of the HX pore and μ the dynamic viscosity. The lower value of *UA* found for AHX2 compared to AHX1 reflects the lower heat transfer area and, presumably, the different influence of the complex flow at the HX junctions on the local heat transfer coefficient. The lower *UA* value leads to higher gas-solid temperature differences and so to higher irreversibility associated to heat transfer.

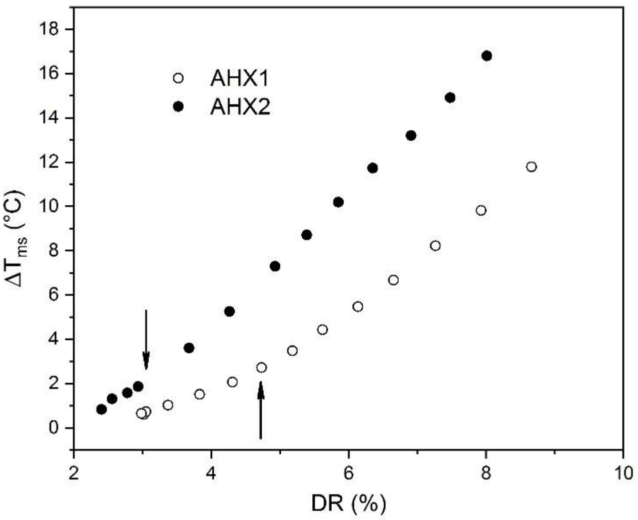

Figure 8. The gas-solid temperature difference as a function of drive ratio for both AHXs.

Vertical arrows in Fig. 8 indicate the pressure amplitude for which the peak-to-peak displacement amplitude ($2\xi_1$) equals the HX length. In both curves the growth of ΔT_{ms} with *DR* seems linear in the *DR* interval below the arrow and faster above. This result could be explained on the basis of the BLC model proposed by Swift which just predicts a linear behavior at low acoustic amplitudes and a squared-one at high acoustic amplitudes as stated by the formula

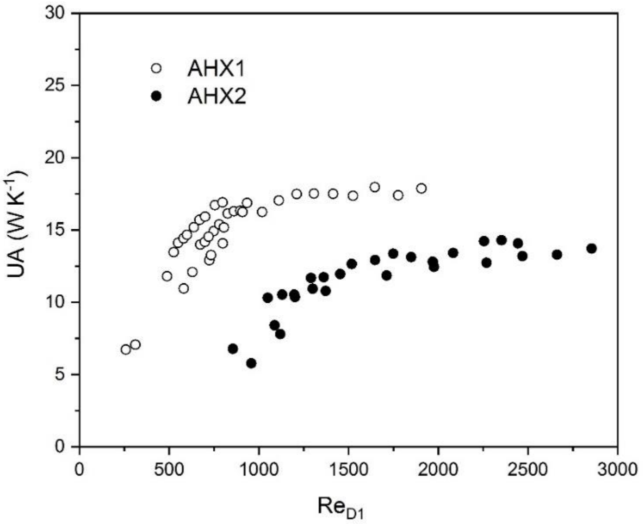

Figure 9. The UA coefficient as a function of the peak Reynolds number for both HXs.

$$\Delta T_{ms} = \frac{\dot{Q} y_{eff}}{KS} = \frac{\dot{Q} R_h}{K A_g} \frac{y_{eff}}{x_{eff}} \qquad (14)$$

where $x_{eff}=\min\{2\xi_1, L_{HX}\}$ and S is the actual gas-solid heat transfer area (proportional to x_{eff}). The predicted behavior takes into account that $\dot{Q} \propto P_A^2$ and that at low acoustic amplitudes (when $2\xi_1 < L_{HX}$) x_{eff} grows as $2\xi_1$ and so proportionally to P_A. This should make ΔT_{ms} to depend linearly on P_A. At high acoustic amplitudes (when $2\xi_1 > L_{HX}$) x_{eff} is constant and equal to L_{HX} and so ΔT_{ms} is expected to exhibit a quadratic dependence on P_A.

In conclusion, the analysis performed in this subsection evidences how AHX2, due to its pore geometry and lower porosity compared to AHX1, is affected by higher irreversibility, both viscous and thermal, which degrades the engine performance.

3.2 Heat transfer correlations

The gas-side heat transfer coefficient estimated as described in section 2.3 and expressed in terms of dimensionless Nusselt number

$$\mathrm{Nu}_D = \frac{hD_h}{K} \tag{15}$$

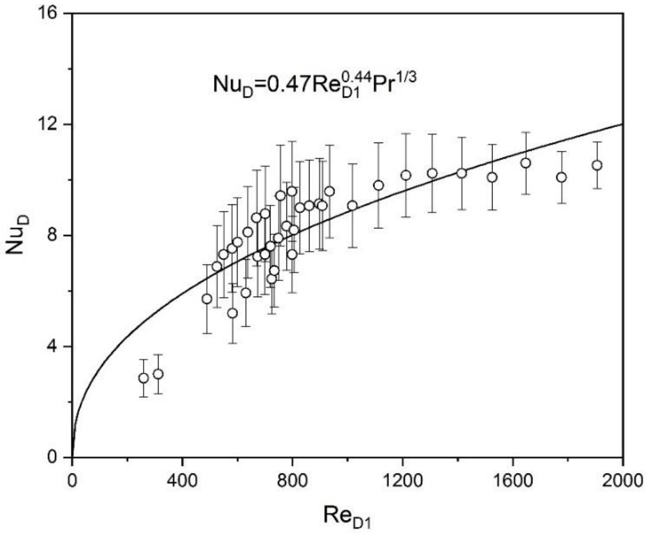

Figure 10. Measured gas-side Nusselt number as a function of acoustic Reynolds number (open circles) for AHX1 and correlation law obtained from data regression (continuous line).

(D_h being the hydraulic diameter of the HX pores) is reported in Fig. 10 as a function of $\mathrm{Re_{D1}}$ (open circles). The graph shows that as $\mathrm{Nu_D}$ increases with $\mathrm{Re_{D1}}$ it reaches a quite constant value above $\mathrm{Re_{D1}} \approx 1200$, where the gas peak-to-peak gas displacement amplitude equals the fin length. The continuous line is a least-squares fit of the experimental points by the function $\mathrm{Nu_D = aRe^b Pr^{1/3}}$ with a coefficient of determination R^2=0.73. The resulting correlation law is

$$\mathrm{Nu}_D = 0.47\,\mathrm{Re}_{D1}^{0.44}\,\mathrm{Pr}^{1/3} \tag{16}$$

In Fig. 11 a comparison with the results of other experimental researches found in literature with regard to HXs of the same configuration (finned-type HXs) is reported.

Nsofor et al. [28] tested a parallel-plate HX made of copper with fin spacing of 0.95 mm and fin thickness of 0.15 mm. The HX worked as the hot HX of a TA refrigerator filled with He at mean pressures ranging from 3 to 8 bar and operation frequencies ranging from 300 to 450 Hz. The heat transfer correlation derived from measurements, after conversion of the rms Re number to peak Re number, is:

$$\mathrm{Nu}_D = 0.548\,\mathrm{Re}_{D1}^{0.31}\,\mathrm{Pr}^{0.11} \tag{17}$$

This function is plotted in Fig 11 as a dotted line.

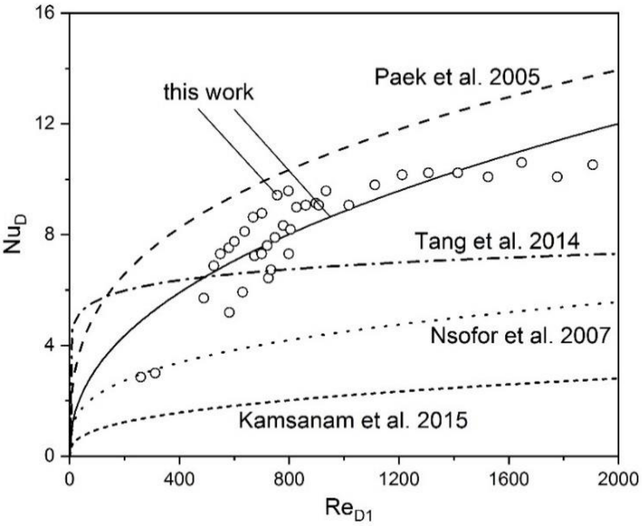

Figure 11. Comparison among the experimental data (open circles) and correlation law (continuous line) obtained in this work for the gas-side Nusselt number and correlation laws experimentally derived by other researchers for heat exchangers of the same type of AHX1.

Paek et al. [29] studied the heat transfer characteristics of finned-tubes HXs made of aluminum with fins spaced 0.54 mm apart. This HX was integrated as cold HX in a TA cooler filled with three He-Ar mixtures (44% He, 33 % He, 22 % He) at three different mean pressures (20, 13.3 and 6.7 bar) and driven near its resonance frequency (136-155.9 Hz). The heat transfer correlation derived from measurements, after conversion of Colburn-*j* factor to Nusselt number, is:

$$\mathrm{Nu}_D = 1.303\,\mathrm{Re}_{D1}^{0.3271}\,\mathrm{Pr}^{1/3} \tag{18}$$

This function is plotted in Fig 11 as a dashed line.

Tang et al. [30] built an experimental apparatus reproducing the operating conditions of pulse tube refrigerators to investigate the heat transfer performance of a finned HX made of copper and cooled by a flow of water through channels surrounding the HX. The fins were 0.75 mm thick, 20 mm long in the flow direction and spaced 0.75 mm apart. The working gas was He at three mean pressures (25, 30 and 35 bar) while the operating frequency varied in the range 40-110 Hz. The test results were summarized in terms of peak Reynold number and Valensi number (Va) as follows

$$\mathrm{Nu}_D = 0.43\,\mathrm{Re}_{D1}^{0.0876}\,\mathrm{Va}^{0.405} \tag{19}$$

where

$$\mathrm{Va} = \frac{\rho_m \omega D_h^2}{\mu} \tag{20}$$

This function (with Va=211 for the experimental conditions of the present study) is plotted in Fig. 11 as a dash-dotted line.

Kamsanam et al. [31] performed measurements of heat transfer on coupled finned-tube HXs (without stack) placed side-by-side in a resonator filled with He. Three HXs made of copper with fin thickness of 0.3 mm, fin length of 20 mm and different fin spacing (0.7, 1.4 and 2.1 mm) were investigated. The correlation obtained from regression of their data, after conversion of Colburn-*j* factor to Nusselt number, is

$$\mathrm{Nu}_D = 0.203\,\mathrm{Re}_{D1}^{0.3606}\,\mathrm{Pr}^{1/3}\left(\frac{t}{D_h}\right)^{-1.2541} \tag{21}$$

t being the fin thickness. This function is plotted in Fig. 11 as a short-dashed line.

The analysis summarized in Fig. 11 reveals that, although all reported correlations refer to the same HX configuration (i.e. a finned-type HX), they are not univocal with very marked deviations which can be as high as 400% as in the case of the correlations proposed by Paek et al. and Kansanam et al. The lower deviation (~ 32%) is found between the correlation derived in the present work and the one proposed by Paek et al [29]. This finding seems to indicate that differences in geometrical parameters (even for HX of the same configuration) and differences in operating conditions (mean pressure, frequency, working fluid, mean temperatures) may have a considerable effect on heat transfer in oscillatory flow. Hence, the definition of general correlation laws applicable to different geometrical configurations and over wide ranges of operating conditions could be an arduous task. This circumstance is well evidenced in the study of Kamsanam et al. [32] where it is found that finned-tube HXs differing uniquely by the plate spacing but working under the same operating conditions are characterized by quite different heat transfer correlation laws.

In Fig. 12 a comparison of the obtained Nusselt number with the predictions of heat transfer models currently applied in thermoacoustics is shown. The models considered here are the BLC, TASFE and RMS-Re models.

The BLC model proposed by Swift [3] and integrated in the DeltaEC code, estimates the heat transfer coefficient by the relation

$$h = \frac{K}{\min\{R_h, \delta_\kappa\}} \tag{22}$$

which is plotted in Fig. 12, after conversion into Nu_D number, as a dotted line.

In the TASFE model classical steady flow heat transfer correlations of the type Nu=Nu(Re, Pr) are converted to the case of oscillatory flows by taking their time average over an acoustic cycle. In the conversion procedure a sinusoidally oscillating velocity, $v_1\sin(\omega t)$, is assumed and substituted for the velocity appearing in the Reynolds numbers of the selected steady flow correlation. The time average over one-half cycle of the resulting time-dependent Nusselt number is then computed:

$$\mathrm{Nu}_{D,TASFE} = \frac{\omega}{\pi}\int_0^{\pi/2} \mathrm{Nu}_D(\mathrm{Re}_{D1}\sin\omega t, \mathrm{Pr})\,dt \tag{23}$$

Similarly, in the RMS-Re model the Reynolds numbers appearing in the steady flow correlation are substituted by their rms values:

$$\mathrm{Nu}_{D,RMS} = \mathrm{Nu}_D(\mathrm{Re}_{D1}/\sqrt{2}, \mathrm{Pr}) \tag{24}$$

The selection from literature of the steady flow correlations to be substituted in the above equations is based on the evidence that in the investigated acoustic Reynolds number range ($\mathrm{Re}_{D1}<2000$) the flow in the HX pores should be laminar [18]. Therefore, the classical correlation for laminar (external) flow over on isothermal plate of length L (already considered by Poese and Garrett [33])

$$\mathrm{Nu}_L = 0.664\,\mathrm{Re}_L^{1/2}\,\mathrm{Pr}^{1/3} \tag{25}$$

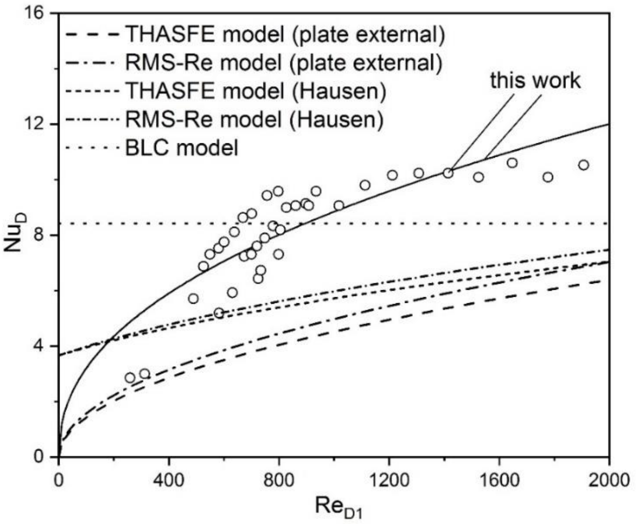

Figure 12. Comparison among the experimental data (open circles) and correlation law (continuous line) obtained in this work for the gas-side Nusselt number and correlation laws predicted by the BLC, THASFE and RMS-Re models (not continuous lines).

and the classical Hausen correlation for laminar (internal) flow in the thermal entry region (L_T) of isothermal ducts

$$\mathrm{Nu}_D = 3.66 + \frac{0.0668(D_h/L_T)\,\mathrm{Pr}\,\mathrm{Re}_D}{1+0.04[(D_h/L_T)\,\mathrm{Pr}\,\mathrm{Re}_D]^{2/3}} \tag{26}$$

are chosen.

Although Eq. (25) refers to external flow it is applied here (with $L=L_{HX}$) because the fins of the investigated HX are not tightly spaced ($R_h/\delta_\kappa\approx 4$). As for Eq. (26) its use could be justified by the fact that, as shown in experimental studies [34], the entrance length for oscillating flows inside stacks is of the order of the displacement amplitude, and so, of the HX length. Based on this evidence, when applying Eq. (26) the heat exchanger fin length has been identified with the thermal entry length ($L_{HX}=L_T$). In Fig 12 the predictions of the TASFE and RMS-Re models are plotted as dashed and dash-dotted lines respectively, as far as the eq. (25) is concerned, and as short-dashed and short-dash dotted lines respectively, as far as eq. (26) is concerned.

The plot shows how the BLC model predicts a constant Nu value, independent of Re_{D1}. The model overestimates the experimental data at $\mathrm{Re}_{D1}<600$ and slightly underestimates them at

Re_{D1}>600. The mean deviation of the predicted Nu_D values from the experimental data amounts to 25%.

The TASFE and RMS-Re models predict the increase of Nu with Re_{D1} but underestimate the experimental values over almost all the investigated Re_{D1} range. The mean deviation of the Nu_D values predicted by the TASFE model from the experimental data amounts to 48% relative to Eq. (25) and to 39 % relative to Eq. (26). The mean deviation of the Nu_D values predicted by the RMS-Re model amounts to 43% relative to Eq. (25) and to 37 % relative to Eq. (26).

In summary, the results of the present study indicate that the BLC model performs better than the TASFE and RMS-Re models based on classical steady-flow correlations in predicting the heat transfer coefficients in oscillating flows. In addition, the RMS-Re modified Hausen correlation works better than the other TASFE and RMS-Re combinations investigated.

Although the BLC model reaches the best agreement with the experimental data of the present work the prediction of a constant Nu_D is in disagreement with the increase of Nu_D at low Re_{D1} values observed in this work and, generally, in all the analogous experimental investigations referred to in this section and deserve further considerations.

The dependence of Nu on Re is usually explained by observing that an increase of Re is associated to an increase of the displacement amplitude and this entails a larger number of gas particles making thermal contact with the HX [28]. This should result in an increase of both the heat exchange area and the gas-solid heat transfer coefficient.

An additional explanation could be formulated if the longitudinal distribution of heat transfer along the HX is taken into account. The BLC model assumes for HXs that the time-averaged solid temperature, gas temperature and thermal gradient along the transverse y direction at the gas-wall interface are constant along the whole extension of the HX (independent of x).

These assumption, however, doesn't agree with the results of numerical studies [7, 8, 13] which found the transverse thermal gradient, and associated heat flux density, to be dependent on the longitudinal direction x. Precisely, the heat flux density is observed to peak at the side of the HX facing the resonator and to change its sign near the HX-stack junction giving rise to local reverse fluxes. These reverse fluxes decrease the net heat transfer between the gas and the HXs, thus worsening the HX performance. These detriment fluxes are found to be active when $2\xi_1 < L_{HX}$. A way to suppress them is to increase the drive ratio (and associated acoustic oscillation amplitude) or, for a fixed drive ratio, to reduce L_{HX} till the condition $2\xi_1 > L_{HX}$ is met. Thus, the growth of Nu_D with Re_{D1} observed in Fig. 10 for $2\xi_1 < L_{HX}$ could simply reflect the progressive reduction of the reverse heat fluxes and the contextual improvement of the HX performance in transferring heat, which leads to higher h (and Nu_D) values.

5. Conclusions

In this paper an experimental investigation on the thermal performance of two TA heat exchangers characterized by a different geometry is performed. With this purpose, a test-rig, consisting of a standing wave engine was built and the HX heat transfer rates were measured over a wide range of velocity amplitudes of the oscillatory flow. The following conclusions can be drawn from the results:

– The HX with circular-pore geometry reduces the performance of the engine compared to the finned-tube HX by about 23%. Due to its circular pore geometry, lower porosity and lower global heat transfer *UA* coefficient, in fact, this heat exchanger works under higher gas-solid temperature differences, which enhances thermal irreversibility associated with heat transfer, and higher acoustic velocity amplitudes, which increases viscous losses and minor losses at the HX-stack and HX-resonator junctions. These sources of irreversibility can seriously degrade the global performance of TA engines.

– The comparison of the experimentally derived dimensionless heat transfer coefficient (Nu number) with analogous experimental works shows that correlation laws derived for different geometrical configurations and operating conditions are not univocal but very marked deviations from each other are typical. This makes the definition of general correlation laws applicable over wide configuration/operation ranges more difficult and indicates that these phenomenologically derived laws may be specific of the investigated case.

– The comparison of the experimentally derived dimensionless heat transfer coefficient (Nu number) with model predictions shows that the TASFE and/or RMS-Re models may introduce significant errors (about 40%) in the estimation of the heat transfer coefficient. The BLC model exhibits the best agreement with the experimental data, with a mean deviation of 25 %. The BLC model also accounts qualitatively for the observed dependence of the gas-solid temperature on drive ratio.

More studies (both theoretical and experimental) are needed to investigate the influence of potential reverse heat fluxes at the HX-stack junction on the growth of the heat transfer coefficient at low acoustic Reynolds number generally observed in all experimental studies.

Funding

This research was funded by the Italian Ministry of University and Research (MIUR): Project number PRIN 2017JP8PHK. The second author would like to thank EPSRC(UK) for funding under HARP2 programme (grant ref. EP/R023328/1).

References

[1] N. Rott, Thermoacoustics, Adv. Appl. Mech., 1980, 20, 135-175 and references therein.

[2] G.W. Swift, Thermoacoustic engines, J. Acoust. Soc. Am., 1988, 84 (4), 1145-1180.

[3] G.W. Swift, Analysis and performance of a large thermoacoustic engine, J. Acoust. Soc. Am., 1992, 92 (3), 1551-1563.

[4] B.L Minner., J.E. Braun, L. Mongeau, Optimizing the design of a thermoacoustic refrigerator, in: International Refrigeration and Air Conditionaing Conference, School of Mechanical Engineering, Purdue University, 1996, pp. 315e322.

[5] N. Cao, J.R. Olson, G.W. Swift, S. Chen, Energy flux density in a thermoacoustic couple, J. Acoust. Soc. Am. 1996, 99 (6), 3456-3464.

[6] H. Ishikawa, D.J. Mee, Numerical investigations of flow and energy fields near a thermoacoustic couple J. Acoust. Soc. Am. 2002, 111 (2), 831-839.

[7] A. Piccolo, Numerical computation for parallel plate thermoacoustic heat exchangers in standing wave oscillatory flow, Int. J. Heat Mass Transf. 2011, 54 (21-22), 4518-4530.

[8] E. Besnoin and O.M. Knio, Numerical study of thermoacoustic heat exchangers in the thin plate limit. Numerical Heat Transfer, Part A, 2001, 40, 445-471.

[9] E. Besnoin and O.M. Knio, Numerical study of thermoacoustic heat exchangers, Acta Acustica United with Acustica, 2004, 90, 432-444.

[10] H. Ishikawa and P.A. Hobson, Optimization of heat exchanger design in a thermoacoustic engine using a second law analysis, International Communications in Heat and Mass Transfer 1996, 23 (6) 325-334.

[11] H. Ishikawa, D.J. Mee, Numerical investigations of flow and energy fields near a thermoacoustic couple, J. Acoust. Soc. Amer. 2002, 111, 831-839.

[12] A. Piccolo, Optimization of thermoacoustic refrigerators using second law analysis, Applied Energy 2013, 103, 358-367.

[13] D. Marx and P. Blanc-Benon, Numerical Simulation of Stack–Heat Exchangers Coupling in a Thermoacoustic Refrigerator, AIAA Journal, 2004, 42, 1338-1347.

[14] M.E.H. Tijani, J.C.H. Zeegers, A.T.A.M. De Waele, Design of thermoacoustic refrigerators, *Cryogenics*, 2002, 42, 49-57.

[15] Z. Yu, A.J. Jaworski, S. Backhaus, Travelling-wave thermoacoustic electricity generator using an ultra-compliant alternator for utilization of low-grade thermal energy, Applied Energy 2012, 99, 135-145.

[16] J.P. Clark, W.C. Ward, G.W. Swift, Design environment for low-amplitude thermoacoustic energy conversion (DeltaEC), *Journal of the Acoustical Society of America* 2007, 122 (5), 3014.

[17] G. Mozurkewich, Heat transfer from transverse tubes adjacent to a thermoacoustic stack, Journal of the Acoustical Society of America 2001, 110 (2) 841-847.

[18] G.W. Swift Thermoacoustics: a unifying perspective for some engines and refrigerators, Acoust Soc Am 2002.

[19] I. Peak, J.E. Braun, L. Mongeau, Characterizing heat transfer coefficients for heat exchangers in standing wave thermoacoustic coolers. *Journal of the Acoustical Society of America*, 2005, 118, 2271-2280.

[20] J.R. Brewster, R. Raspet, H.E. Bass, Temperature discontinuities between elements of thermoacoustic devices, J. Acoust. Soc. Am. 1997, 102 (6), 3355-3360.

[21] E.C. Nsofor, S. Celik, X. Wang, Experimental study on the heat transfer at the heat exchanger of the thermoacoustic refrigerating system, Appl. Therm. Eng. 2007, 27 (14-15) 2435-2442.

[22] A.J. Jaworski, A. Piccolo, Heat transfer processes in parallel-plate heat exchangers of thermoacoustic devices–numerical and experimental approaches, *Applied Thermal Engineering*, 2012, 42, 145-153.

[23] K. Tang, Yu J., T. Jin, Y.P. Wang, W.T. Tang, Z.H. Gan, Heat transfer of laminar oscillating flow in finned heat exchanger of pulse tube refrigerator, Int. J. Heat Mass Transf. 2014, 70, 811-818.

[24] W. Kamsanam, X. Mao, A.J. Jaworski, Development of experimental techniques for measurement of heat transfer rates in heat exchangers in oscillatory flows, Experimental Thermal and Fluid Science 2015, 62, 202-215.

[25] F.P. Incoprera, D.P. De Witt, 1996, Fundamentals of Heat and Mass Transfer, third ed., Wiley and Sons, New York.

[26] L. Shi, Z. Yu, A.J. Jaworski, Vortex shedding flow patterns and their transitions in oscillatory flows past parallel-plate thermoacoustic stacks, Experimental Thermal and Fluid Science 2010 (34) 954-965

[27] K.I. Matveev, G.W. Swift, S. Backhaus, Temperatures near the interface between an ideal heat exchanger and a thermal buffer tube or pulse tube, International Journal of Heat and Mass Transfer 2006 (49) 868-878

[28] E.C. Nsofor, S. Celik, X. Wang, Experimental study on the heat transfer at the heat exchanger of the thermoacoustic refrigerating system, Appl. Therm. Eng. 2007 (27) (14-15) 2435-2442.

[29] I. Paek, J.E. Braun, L. Mongeau, Characterizing heat transfer coefficients for heat exchangers in standing wave thermoacoustic coolers, J. Acoust. Soc. Am. 2005 (118) (4) 2271-2280.

[30] K. Tang, J. Yu, T. Jin, Y.P. Wang, W.T. Tang, Z.H. Gan, Heat transfer of laminar oscillating flow in finned heat exchanger of pulse tube refrigerator, Int. J. Heat Mass Transf. 2014 (70) 811-818.

[31] W. Kamsanam, X. Mao, A.J. Jaworski, Development of experimental techniques for measurement of heat transfer rates in heat exchangers in oscillatory flows, Exp. Therm Fluid Sci. 2015 (62) 202-215.

[32] W. Kamsanam, X. Mao, A.J. Jaworski, Thermal performance of finned-tube heat exchangers in oscillatory flow conditions. International Journal of Thermal Sciences 2016 (101) 169-180.

[33] M.E. Poese, S.L. Garrett, Performance measurements of a thermoacoustic refrigerator driven at high amplitudes. Journal of the Acoustical Society of America 2000 (107) (5) 2480-2486.

[34] A.J. Jaworski, X. Mao, X. Mao, Z. Yu, Entrance effects in the channels of the parallel plate stack in oscillatory flow conditions, Experimental Thermal and Fluid Science 2009 (33) 495-502.

Highlights

- The thermal performance of finned-tube and circular-pore heat exchangers is studied.
- The effect of pore geometry and porosity on engine performance is assessed.
- Finned-tube heat exchanger improves engine performance due to lower irreversibility.
- The dimensionless heat transfer coefficient vs acoustic Reynolds number is measured.
- The Boundary Layer Conduction model has the best agreement with experimental data.

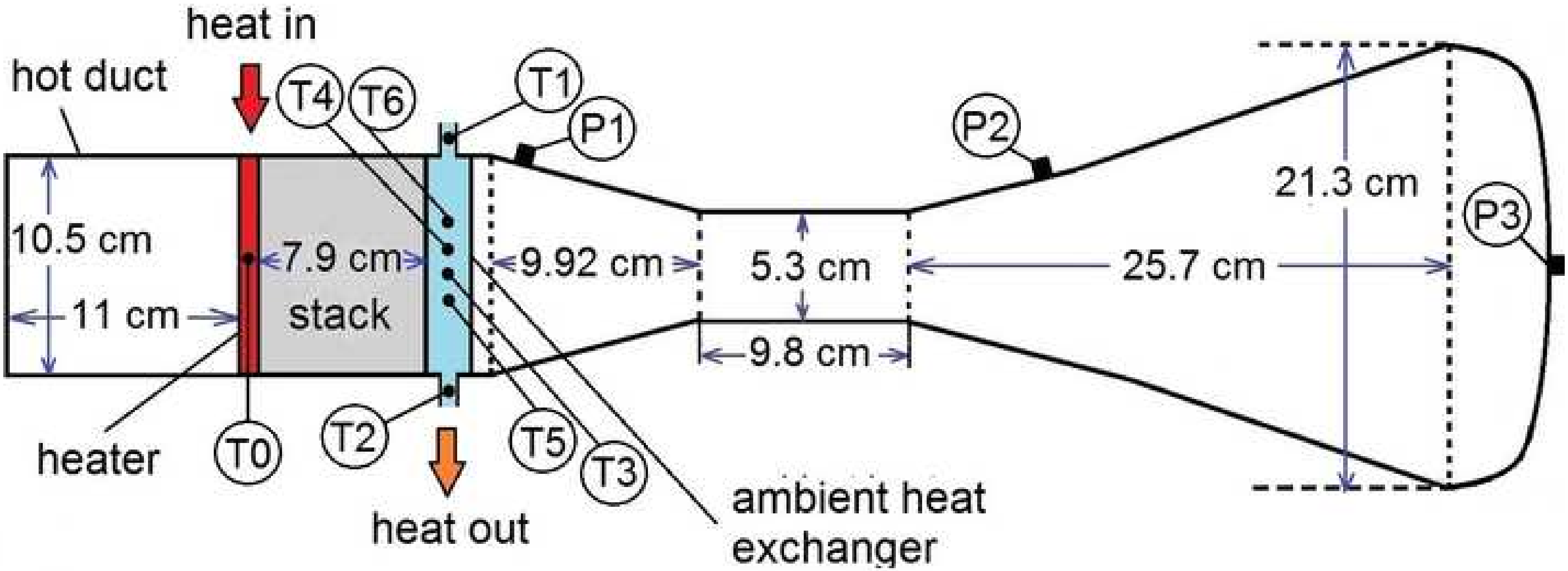
heat in
hot duct
T4
T6
T1
P1
P2
P3
10.5 cm
7.9 cm
9.92 cm
5.3 cm
25.7 cm
21.3 cm
11 cm
stack
9.8 cm
heater
T0
T2
heat out
T5
T3
ambient heat exchanger

Click here to access/download;Figure;Figure 02.jpg

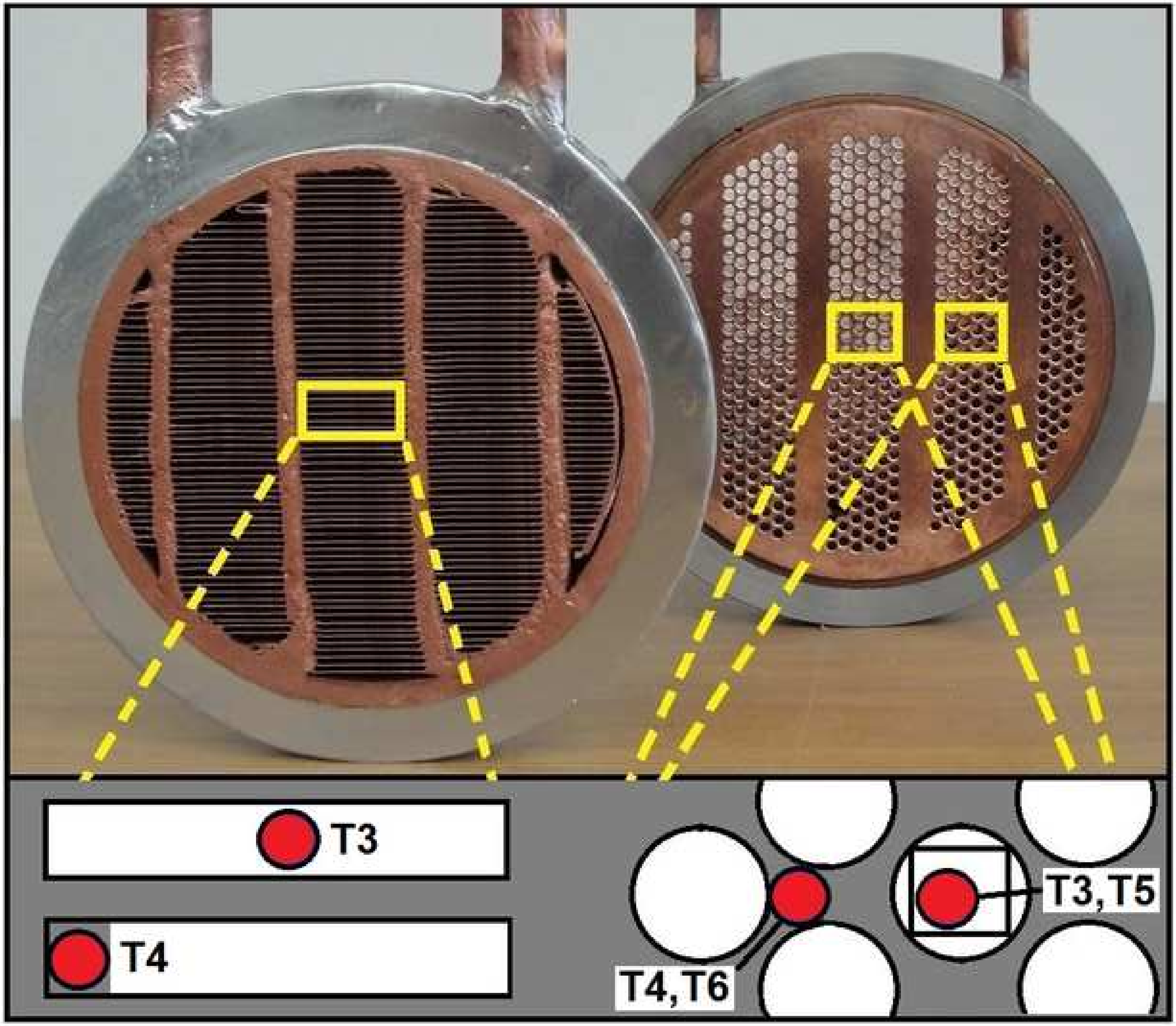

Click here to access/download;Figure;Figure 03.jpg

Click here to access/download;Figure;Figure 04.jpg

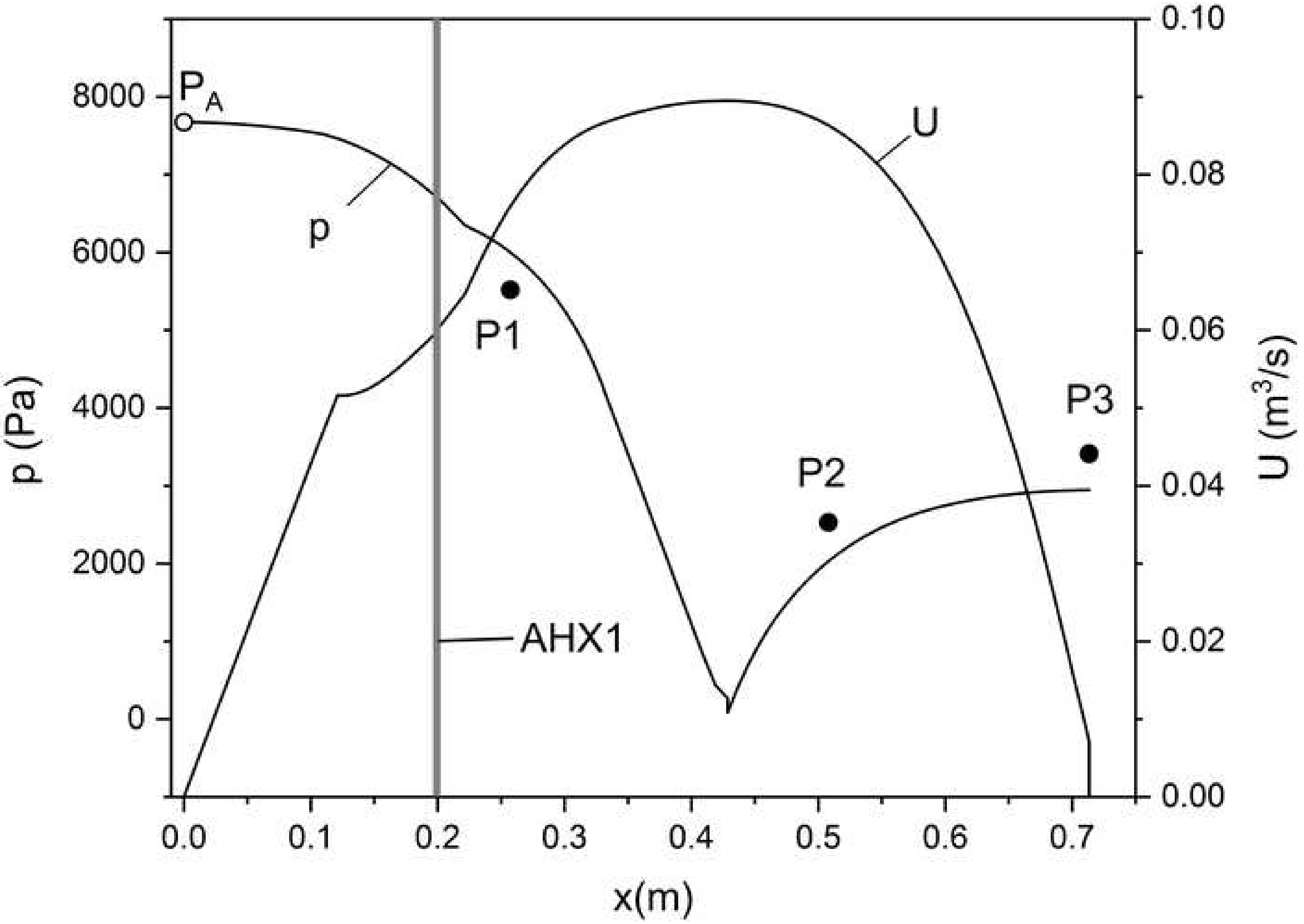

Click here to access/download;Figure;Figure 05.jpg

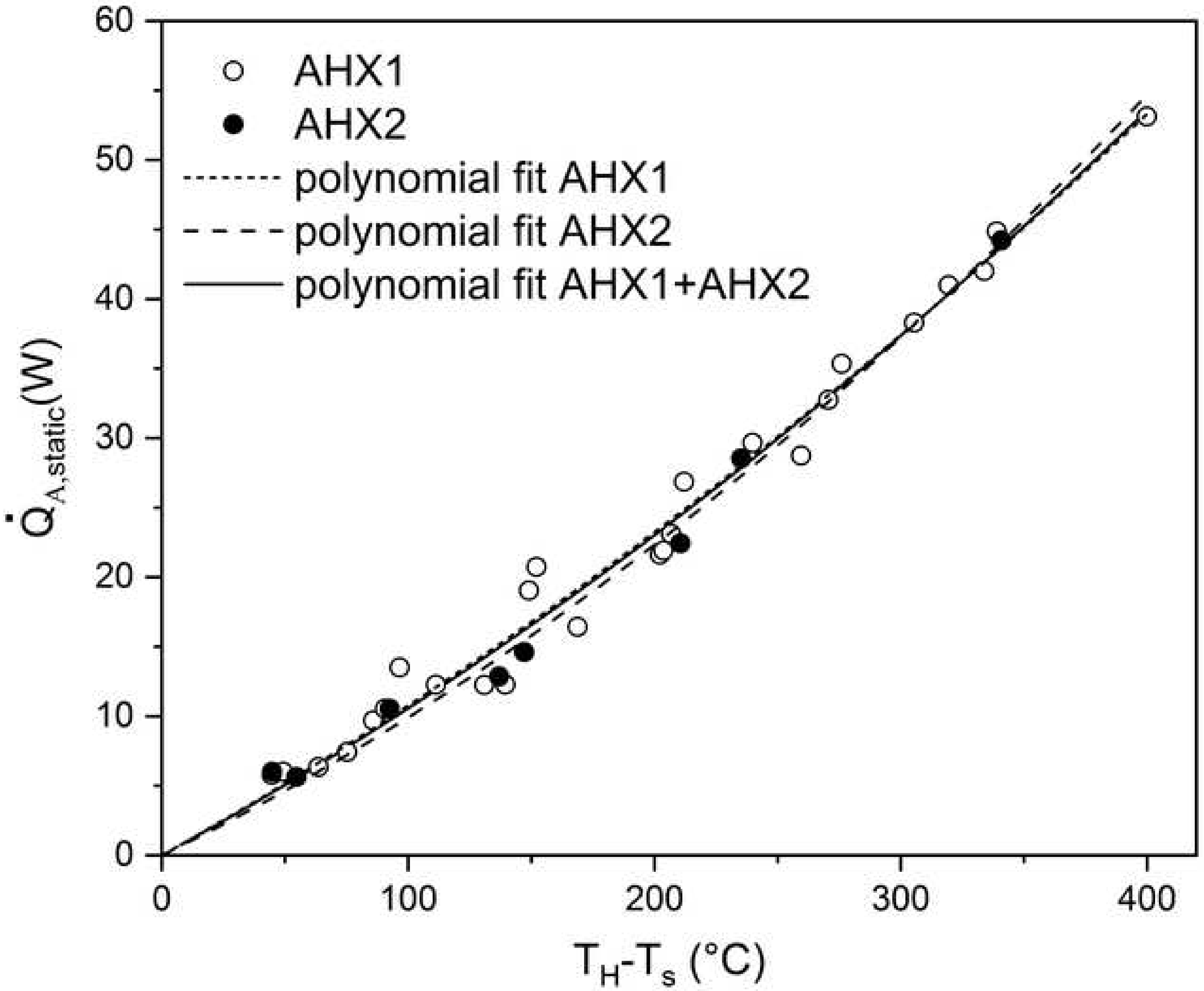

Click here to access/download;Figure;Figure 06.jpg

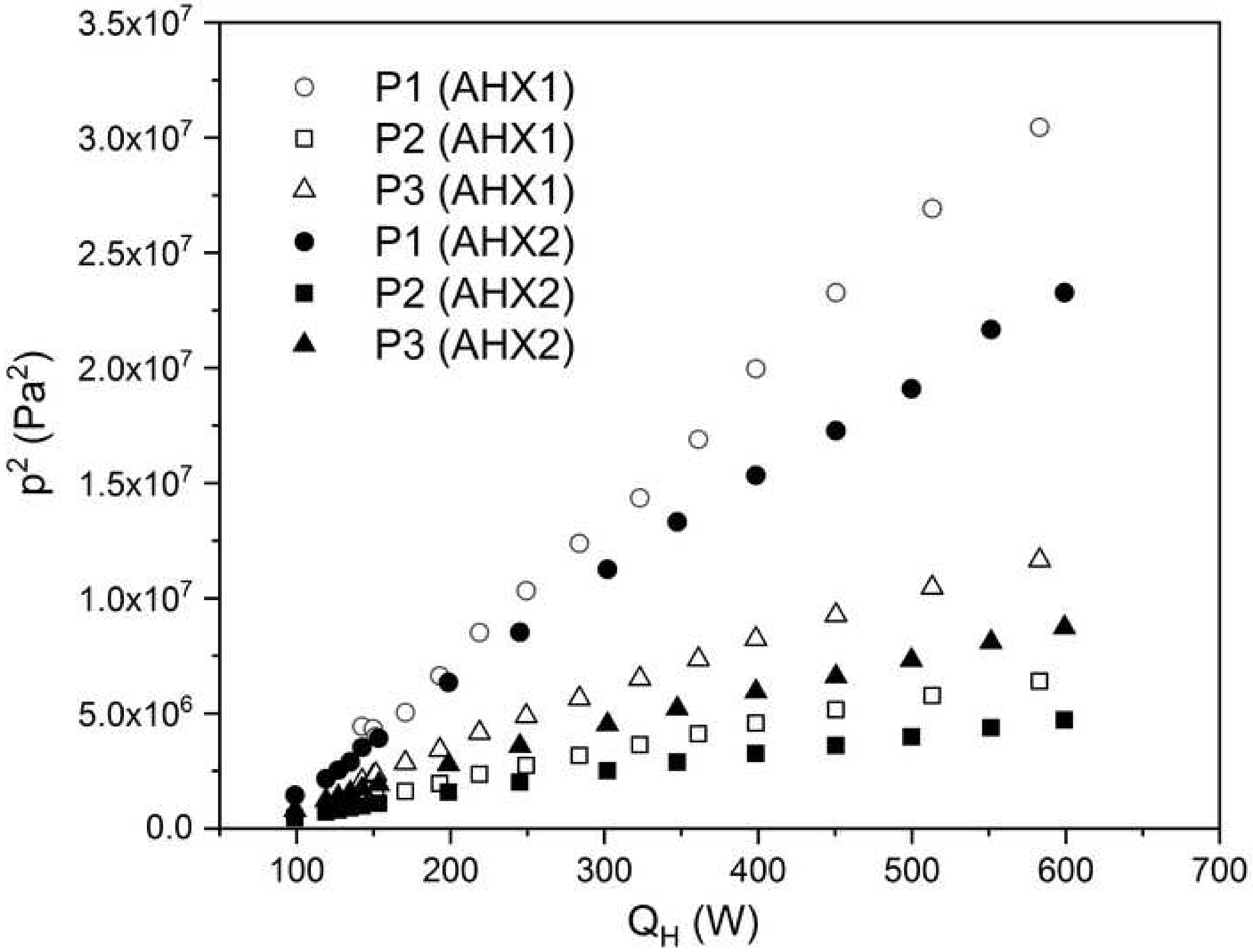

Click here to access/download;Figure;Figure 07.jpg

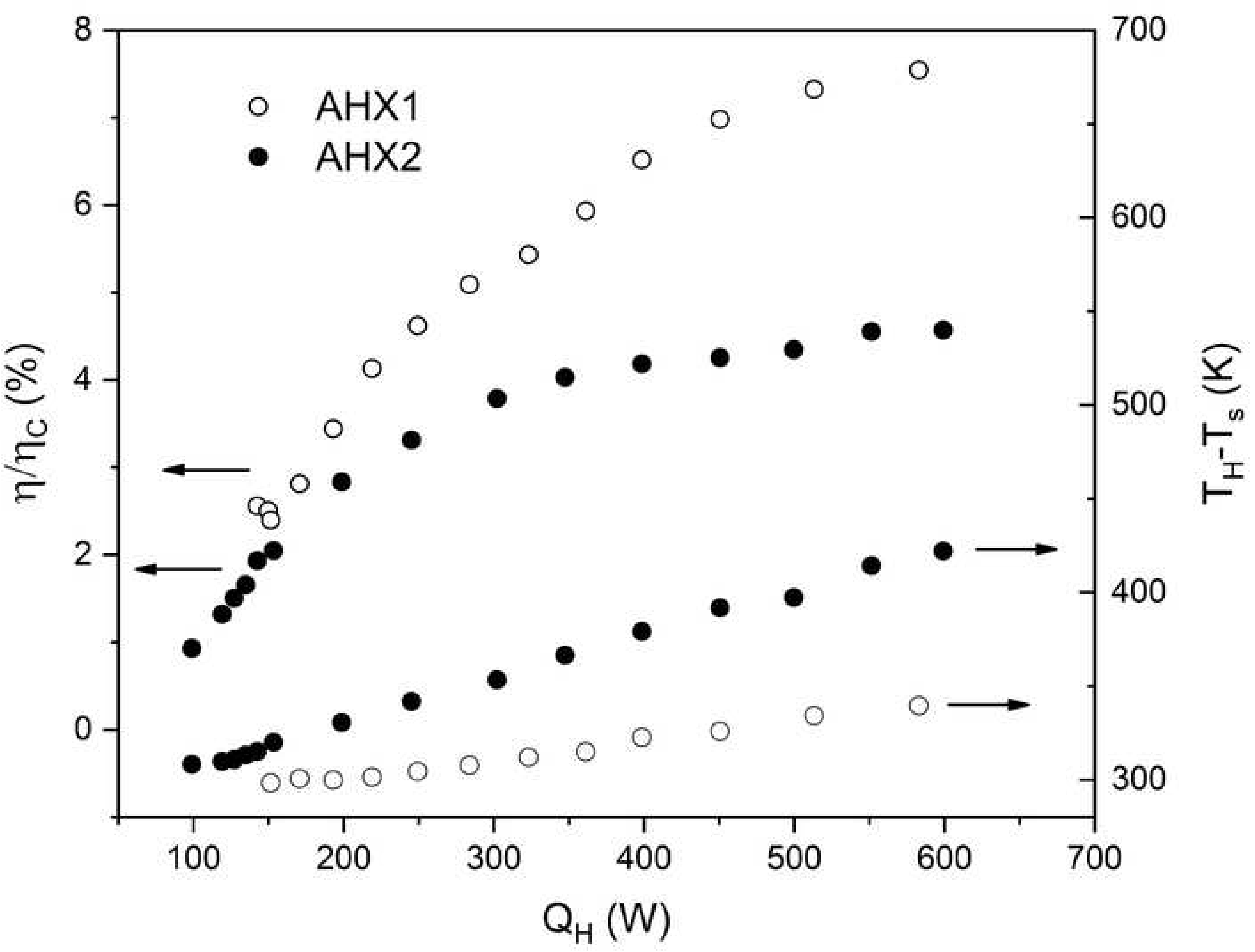

Click here to access/download;Figure;Figure 08.jpg

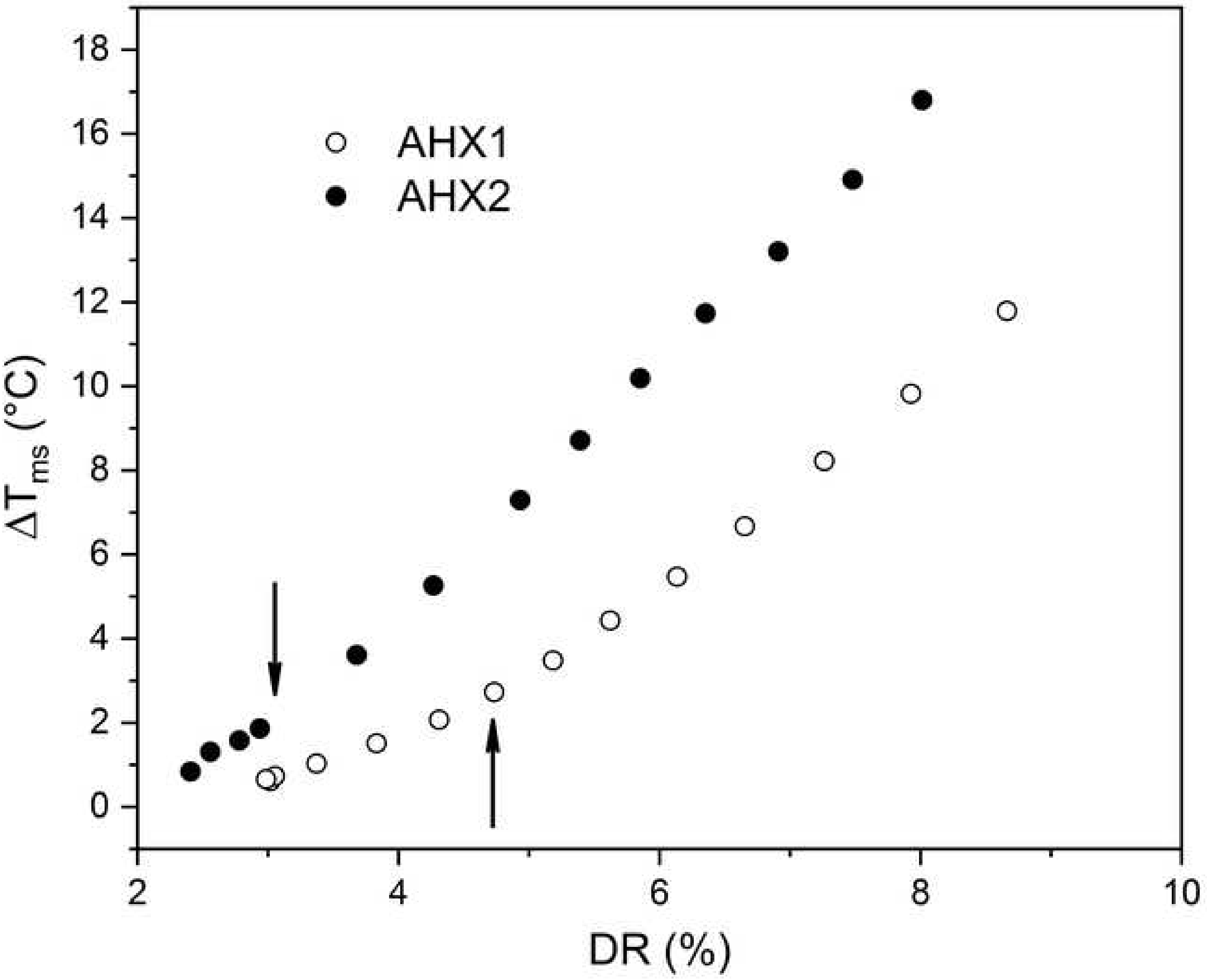

Click here to access/download;Figure;Figure 09.jpg

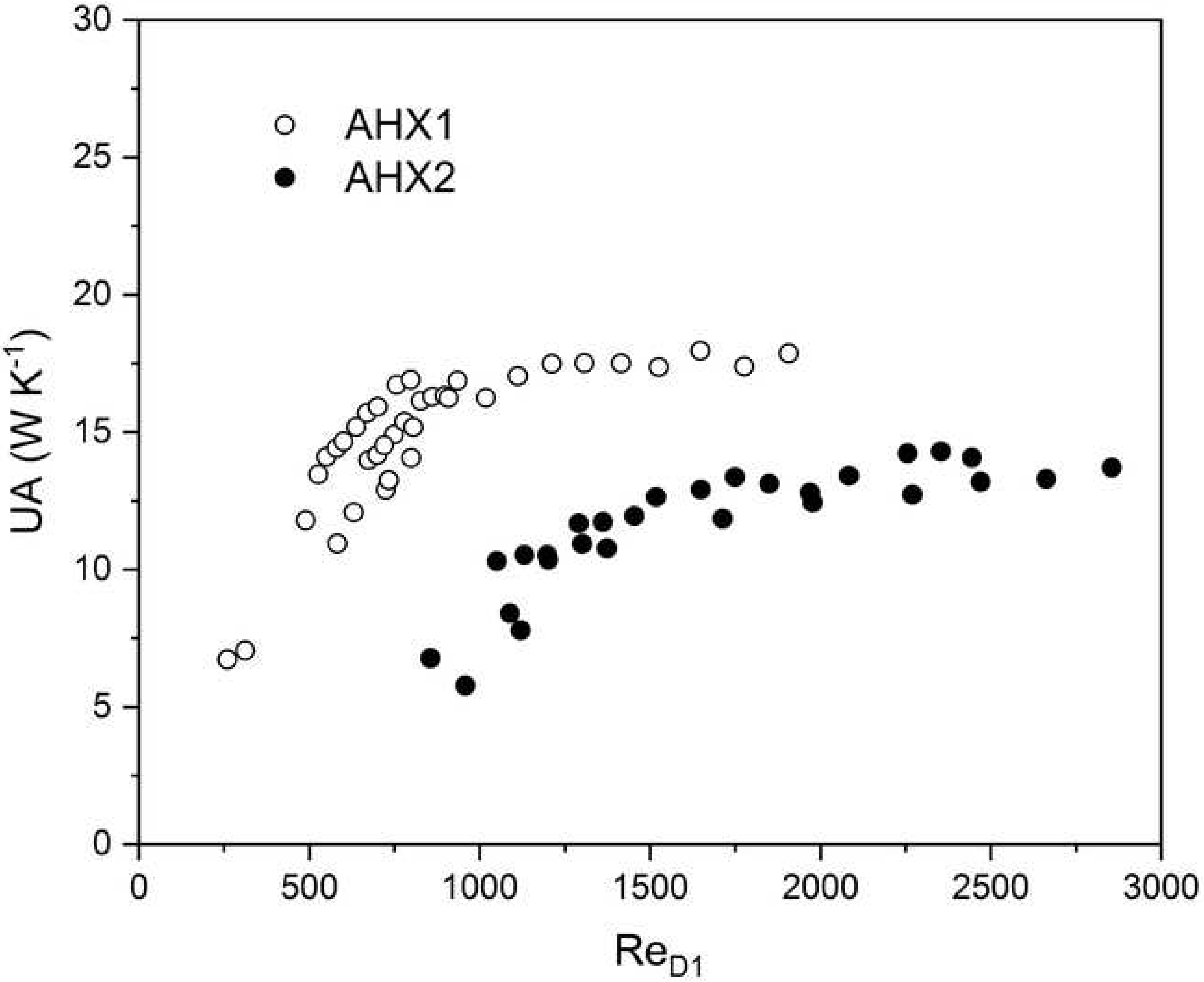

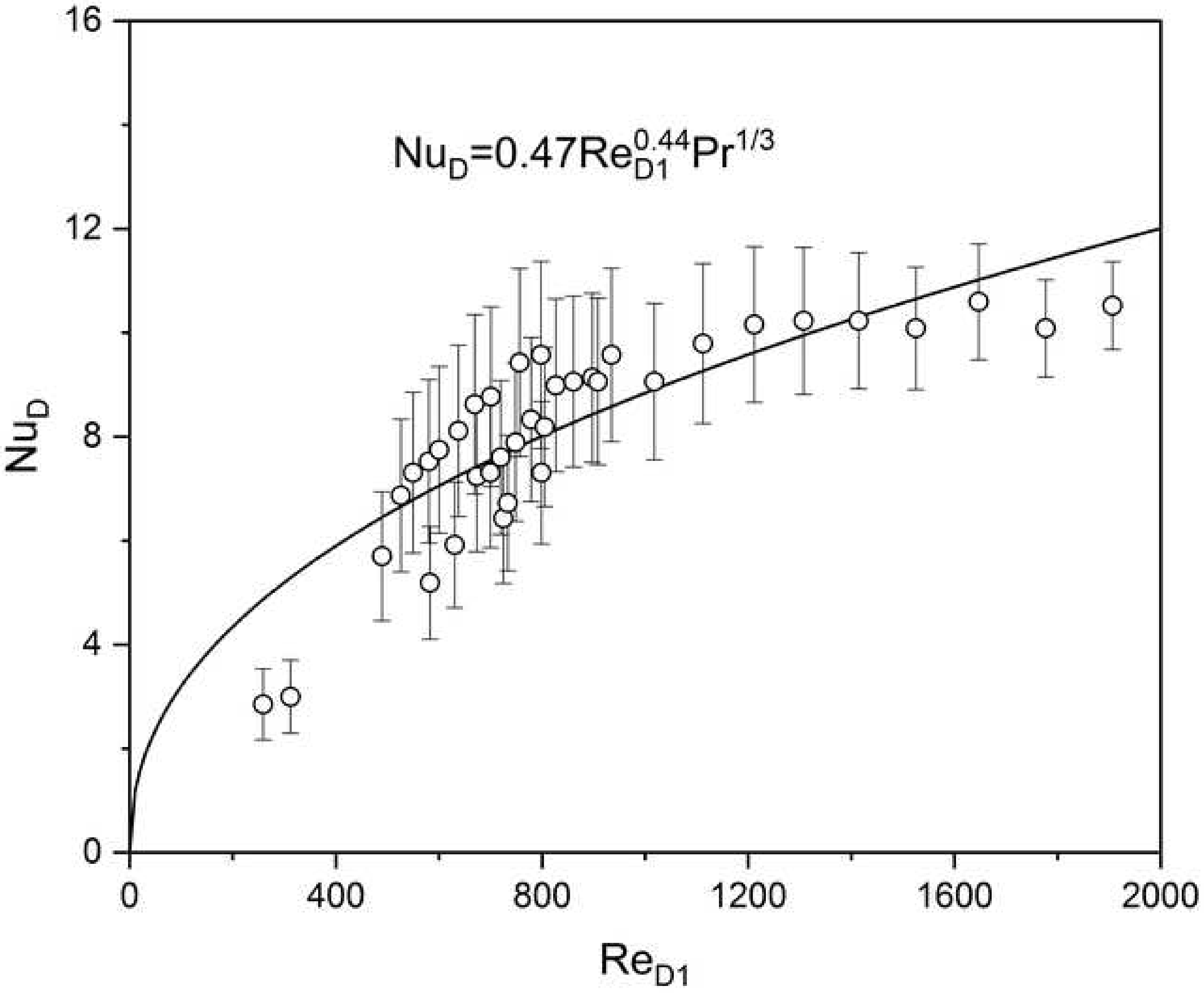
$Nu_D=0.47Re_{D1}^{0.44}Pr^{1/3}$
16
12
8
4
0
Nu_D
0
400
800
1200
1600
2000
Re_{D1}

Click here to access/download;Figure;Figure 11.jpg

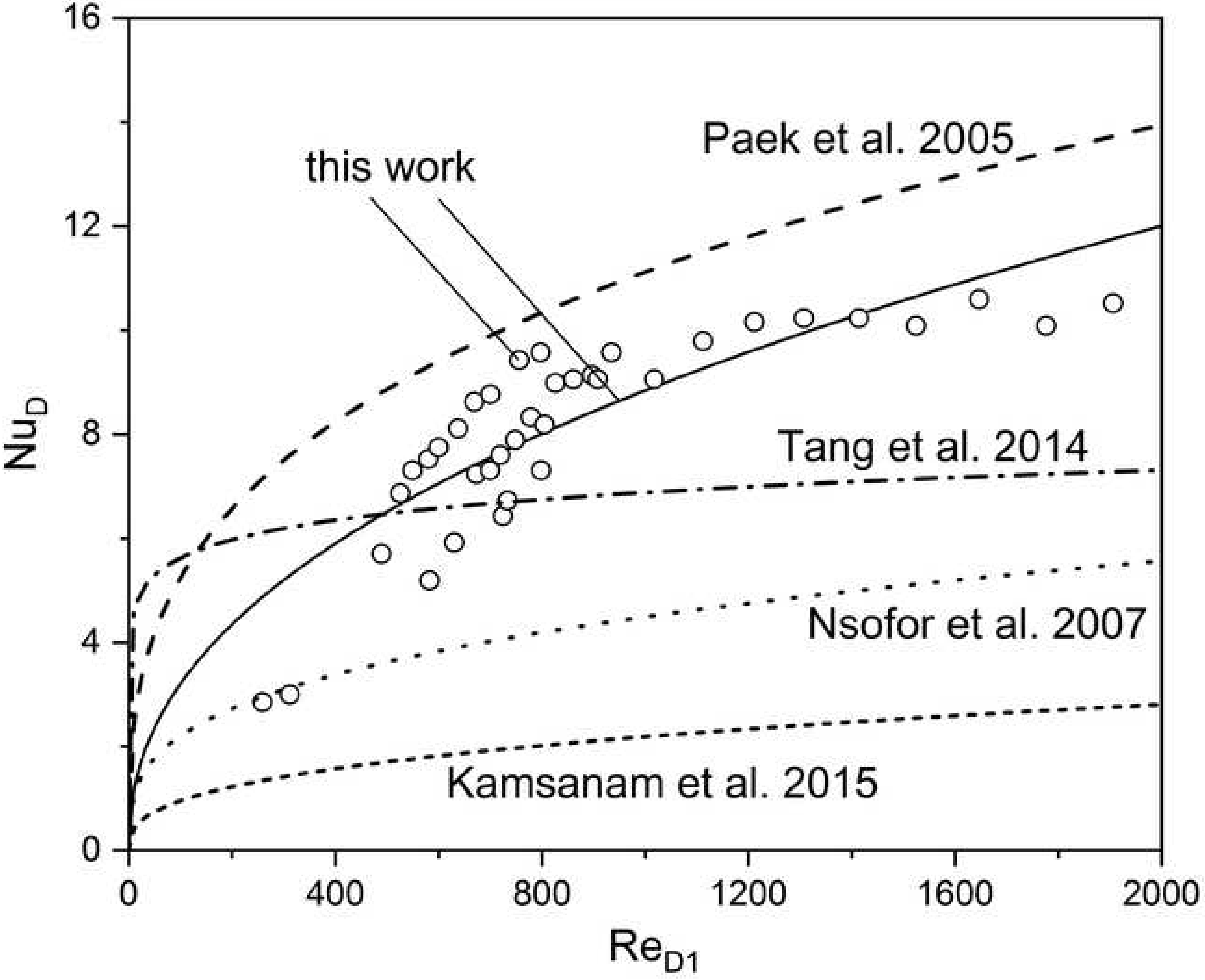

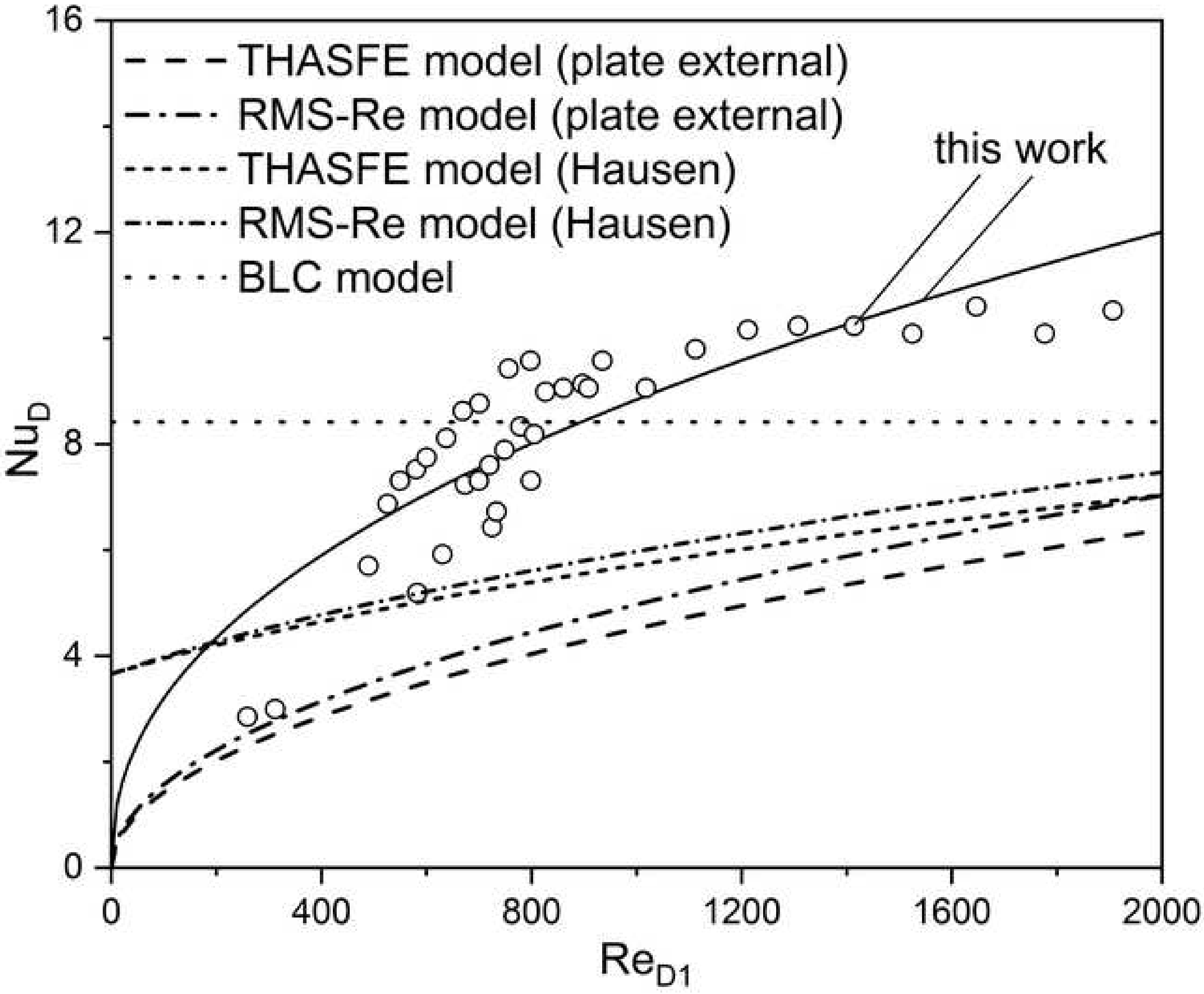
THASFE model (plate external)
RMS-Re model (plate external)
THASFE model (Hausen)
RMS-Re model (Hausen)
BLC model
this work
16
12
8
4
0
Nu_D
0
400
800
1200
1600
2000
Re_{D1}

Declaration of interests

☒ The authors declare that they have no known competing financial interests or personal relationships that could have appeared to influence the work reported in this paper.

☐The authors declare the following financial interests/personal relationships which may be considered as potential competing interests:

Experimental study of heat transfer characteristics of finned-tube and circular-pore heat exchangers in oscillatory flow

Antonio Piccolo(a)(*), Artur J. Jaworski(b)

(a)*Department of Engineering, University of Messina, Contrada di Dio, 98166 S. Agata (Messina) Italy*
(b)*School of Computing and Engineering, University of Huddersfield, Huddersfield, HD1 3DH, UK*

Abstract. This work is concerned with an experimental investigation of the thermal performance of two thermoacoustic heat exchangers characterized by different pore geometries, namely a circular-pore geometry and a finned-tube geometry. A standing wave engine, where the heat exchangers under test play the role of ambient HXs, is used as test-rig. Heat transfer rates measurements by standard energy balance techniques and dynamic pressure measurements are used to assess the impact of the two heat exchangers on the engine performance. The gas-side heat transfer coefficient, expressed as Nusselt number, is also determined for the finned-tube heat exchanger. The resulting values are compared to the heat transfer coefficients estimated in analogous experimental studies and by predictive models. Results show that the circular-pore heat exchanger reduces the performance of the engine compared to the finned-tube heat exchanger by about 23%, being affected by higher thermal and viscous irreversibility. Moreover, the boundary layer conduction model exhibits a better agreement with the measured heat transfer coefficients compared to other models. A new correlation law, based on regression of the experimental data, is also derived.

Keywords: Thermoacoustics; Heat exchangers; Heat transfer; Oscillatory flow

(*) **Corresponding author. Tel**.: +39 090 6765311, **email**: apiccolo@unime.it

Highlights

- The thermal performance of finned-tube and circular-pore heat exchangers is studied.
- The effect of pore geometry and porosity on engine performance is assessed.
- Finned-tube heat exchanger improves engine performance due to lower irreversibility.
- The dimensionless heat transfer coefficient vs acoustic Reynolds number is derived.
- The Boundary Layer Conduction model has the best agreement with experimental data.

Nomenclature

A	total cross section area, m^2
A_f	fin cross section area, m^2
A_g	cross section area open to gas flow, m^2
AHX	ambient heat exchanger
A_1, A_2	empirically fitted parameters
c_w	water specific heat, J/kgK
d	tube wall thickness, m
D_h	hydraulic diameter, m
DR	drive ratio (P_A/P_m)
f	frequency, Hz
g	HX-stack separation gap, m
h	gas-side heat transfer coefficient, W/m^{2}K
h_w	water-side heat transfer coefficient, W/m^{2}K
K	gas thermal conductivity, W/mK
K_f	fin thermal conductivity, W/mK
K_t	tube thermal conductivity, W/mK
L	plate length, m
L_f	half fin length, m
L_{HX}	heat exchanger length, m
L_T	thermal entry length, m
m	fin parameter
Nu	Nusselt number
p	acoustic pressure (Pa)
P_A	pressure amplitude at a pressure antinode, Pa
P_m	mean pressure, Pa
Pr	Prandtl number
P1,..,P3	pressure sensors
$\dot{Q}$	convective heat transfer rate, W
$\dot{Q}_A$	AHX heat transfer rate, W
$\dot{Q}_H$	input heat transfer rate, W
$\dot{Q}_{K1}, \cdot\dot{Q}_{K3}$	conductive heat transfer rate, W
$\dot{Q}_{leak}$	leakage heat transfer rate, W
Re	acoustic Reynolds number
R_h	hydraulic radius, m

T1,..,T6	temperature sensors
U	volumetric velocity, m^3/s
UA	overall heat transfer coefficient, W/K
$\dot{V}$	water volume flow rate, m^3/s
Va	Valensi number
v_1	local velocity amplitude, m/s
W_a	acoustic power, W
x	axial irection, m
x_{eff}	min{$2\xi_1$, L_{HX}}
y_{eff}	min{R_h, δ_κ}

Greek symbols

Δ	difference
ΔT_{ms}	gas-solid temperature difference, K
δ_κ	thermal penetration depth, m
η	engine efficiency
η_C	Carnot's efficiency
η_f	fin efficiency
θ_{ml}	log-mean temperature difference, K
κ	gas thermal diffusivity, m^2 s^{-1}
μ	dynamic viscosity, Ns/m^2
ξ_1	displacement amplitude, m
Π	fin cross-section perimeter, m
ρ_m	gas density, kg/m^3
ρ_w	water density, kg/m^3
ϕ	porosity
ω	angular frequency, rad/s

Subscripts

A	ambient, peak amplitude
D	diameter
f	fin
g	gas
H	hot, heater

S	gas-solid heat transfer area, m^2
S_b	unfinned surface area, m^2
S_w	inner tube surface, m^2
t	fin thickness, m
T_H	heater temperature, K
T_m	local gas temperature, K
T_s	temperature at the fin base, K
T_1, T_2	inlet/outlet water temperature, K
T_2'	corrected outlet temperature of water, K

HX	heat exchanger
L	length
m	mean
RMS	Root Mean Square Reynolds Number
static	static measurement
TASFE	Time-Average Steady-Flow Equivalent
w	water
1	first-order acoustic variable

1. Introduction.

In thermoacoustic (TA) engines the heat exchanger (HX) plays the fundamental role of providing the heat transfer between external thermal reservoirs and the core of the engine, namely a porous media of high thermal capacity (stack/regenerator) where the heat/sound energy conversion takes place. Although the theoretical foundations of TA energy conversion were formulated by Rott in the seventies of last century [1] the design methodologies of this component are not yet well-established.

The main issues involved in its design arise from it working under oscillatory flows with short acoustic displacement. This fact has two important implications: (a) the heat transfer area cannot be increased by simply increasing the HX length along the direction of the acoustic oscillation; (b) standard steady flow correlations for compact HXs cannot be directly applied. The first point demands for clear rules on selection of the optimal geometrical configuration of the HX (length, pore hydraulic radius etc.) for a given application. The last point demands for reliable heat transfer correlations specific to oscillatory flows in the dynamic range typical of TA engines. Both theoretical and experimental approaches were applied to investigate the above issues.

As for the first issue, the basic design rule of TA HXs was first given by Swift [2] who argued that the length of the HXs (L_{HX}) along the direction of acoustic oscillation (x-direction thereafter) should be of the order of (and not exceed) the peak-to-peak displacement amplitude ($2\xi_1$). In a later research Swift [3] found experimental evidence of improvement in engines' performance for HXs of reduced length ($\sim\xi_1$). It is also suggested that the hydraulic radius of the HX pores, R_h, should be of the order of the thermal penetration depth (δ_κ), which represents the distance over which heat diffuses in an acoustic cycle. This statement derives from considering that the gas responsible for heat transport to/from the stack oscillates at a distance δ_κ from the gas-solid boundary. Analogously, Minner et al. [4] found, on the basis of an optimization study of TA refrigerators, that the optimal value of the normalized distance R_h/δ_κ should range from 2 to 4.

Cao et al. [5] evidenced, through numerical simulation of parallel-plate stacks, that the lengths L_{HX} and R_h are correlated: the smaller the pore hydraulic radius the shorter the HX length. This result, also found in other computational investigations [6-7], indicates that the length of HXs with small pores ($R_h/\delta_\kappa<1$) could be shorter than $2\xi_1$ and about equal to the particle displacement distance (ξ_1). Even lower values ($L_{HX}/\xi_1 \sim 0.6$) were found by Besnoin and Knio [8] although the same authors found lengths exceeding $2\xi_1$ in a subsequent study [9].

Entropy generation minimization methods [10-12] showed that the above correlation should result as a trade-off between the thermal irreversibility associated with heat transfer and the irreversibility associated with viscous and thermal dissipation. This trade-off, producing a minimum in entropy generation, happens at lower L_{HX} values as R_h is reduced due to quadratic increase of the viscous dissipation with R_h for $R_h \to 0$.

The numerical studies of Besnoin and Knio [8, 9] and Marx and Blanc-Benon [13] evidenced that, in addition to L_{HX} and R_h, the separation gap g between a stack and the adjacent HX could have a considerable influence on the HX performance. In a real TA device this gap minimizes adverse thermal conduction from the hot to the cold HX and prevents the HX to obstruct the regenerator/stack pores. The optimal gaps found in these studies at the investigated configurations lie in the range 0.12–0.2 ξ_1.

The effect of difference in porosity ϕ (defined as the ratio of cross-section area open to gas flow, A_g, to total area, A) between the HX and adjacent stack is considered [4] to be responsible of complex turbulent flow patterns which actually increase the friction losses at the junction [3]. To avoid these adverse entrance problems Tijani et al. [14] suggested that the porosity of the HX should match the porosity of the stack. This recommendation, formulated for standing wave devices, could not be fully applicable to travelling wave devices where the HX porosity is in some cases set to produce deliberate phase shifting of the acoustic wave [15].

Optimal design of TA HXs entails therefore setting proper values of the four geometrical parameters L_{HX}, R_h, g, ϕ, but clear and univocal guidelines establishing how these parameters must be related in an optimized configuration have not been to date formulated.

As for the second issue, the calculation of the gas-side heat transfer coefficient h relies principally on the model formulated by Swift [3], the so called "Boundary Layer Conduction" (BLC) model (also integrated in the design code "DeltaEC" [16]). This model states $h=K/y_{eff}$ where K is the gas thermal conductivity and y_{eff} is the minimum between R_h and δ_κ.

Other relevant models are the "Time-Average Steady-Flow Equivalent" (TASFE) [17] and the "Root Mean Square Reynolds Number" (RMS-Re) [18] models which similarly try to derive non-dimensional heat transfer correlations for the TA case by time averaging over an acoustic cycle classical steady-flow correlations.

A number of experimental investigations, involving different HX geometries and test conditions, were carried out to validate the above models and to define robust correlations for the estimation of h in oscillatory flows [19-24]. The results reported in these studies indicate that the application of the TASFE and RMS-Re models may introduce significant errors in predicting the h value. Furthermore, the experimentally derived correlations are ambiguous and configuration dependent.

The above discussion show how current knowledge on the design of efficient HXs for TA applications is not yet exhaustive. As a result, additional research is needed to investigate on the impact of HX geometry on heat transfer and to develop reliable correlations for the determination of the gas-side heat transfer coefficient under oscillatory flow conditions.

With this purpose in this paper the results of an experimental research aimed at studying the impact of two HXs characterized by a different geometry (circular and finned) on the global thermoacoustic system performance and at deriving (in the finned geometry case) proper heat transfer correlations are presented. The test-rig is a TA engine of the standing-wave type where the investigated HXs play the role of ambient HXs. Engine performance and HXs heat transfer rates are determined over a wide range of velocity amplitudes through standard sound pressure and energy balance measurements. The derived correlation law, expressed in terms of Nusselt number, is then compared to analogous measurements found in literature and to the predictions of the models discussed above.

2. Experimental setup and data reduction.

2.1 Experimental apparatus

The test-rig considered for this research consists of a standing wave thermoacoustic engine using air at atmospheric pressure as working fluid. It is characterized by a resonance frequency of 143.2

Hz and by an onset temperature difference of about 350 °C. A schematic of the engine is shown in Fig. 1.

The resonator is made of stainless steel and comprises a “hot” duct with a diameter of 10.5 and 10 cm long, a “stack holder” with a diameter of 10.5 cm and 8 cm long, a conical shaped segment (taper angle ~15°), a narrow duct with a diameter of 5.3 cm and 20 cm long and a buffer volume (a closed conical shaped duct with taper angle ~15°).

The stack is a ceramic (cordierite) honeycomb stack 7.9 cm long in the *x* direction. The pores have a squared shape with R_h=0.28 mm while the cell density is near 400 cpsi.

The electric heater is fabricated by wrapping about 3.7 m of a Ni-Cr wire (12 Ω/m) uniformly in and out the pores of a honeycomb ceramic slice 1 cm long in the *x* direction (and made of the same material of the stack) that served as a support. A 2 cm long stainless-steel ring equipped with feedthroughs for power cables is used to accommodate the slice.

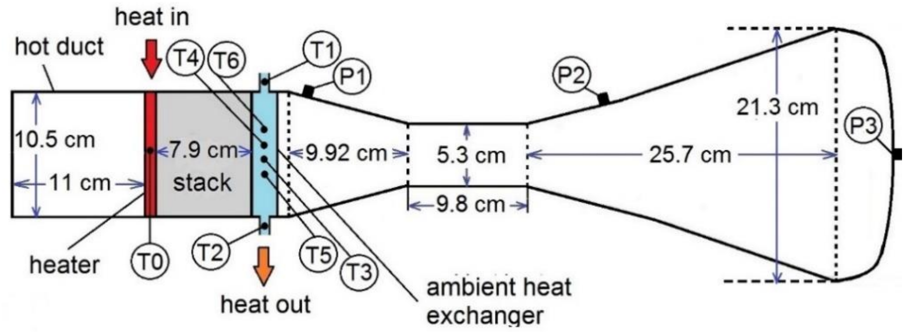

Figure 1. Schematic of the standing wave test engine. Labels “T” indicate thermocouple location. Labels “P” indicate microphone location.

The HXs under test are two cross-flow HXs with four water-tube passes. A picture of the two HXs, which in the engine arrangement work as ambient HXs, is shown in Fig. 2.

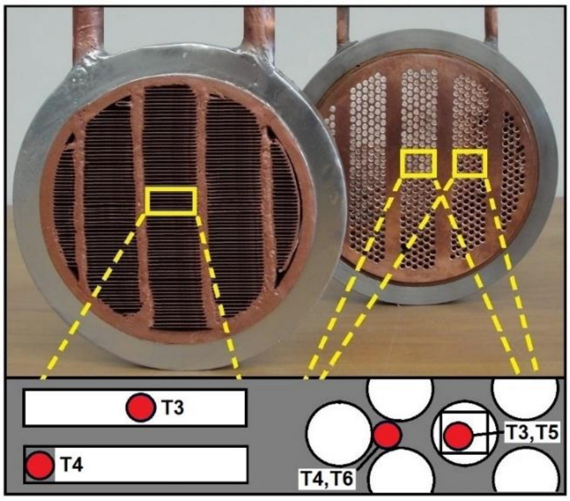

Figure 2. The heat exchanger with finned-tube (on the left) and circular-pore (on the right) geometry. Red circles indicate thermocouples.

The first HX (AHX1) is of the finned-tube type. It is 2 cm long in the *x* direction. For its fabrication a copper ring 2 cm thick with an internal radius of 10.5 cm and an external radius of

14 cm was used as mechanical support of the HX itself. Just outside the HX the cooling water flows through a copper tube with a diameter of 14 mm which has been crushed to obtain a rectangular cross section pipe of area 2 cm×0.5 cm. The crushed pipe has then been bent six times to allow for four passages in the front section of the HX as shown in Fig. 2. The fins are made of strips of laminated copper 0.45 mm thick and 2 cm wide. These strips have been welded to the external walls of the pipe with a fin spacing of 1.1 mm (resulting in R_h=0.55 mm). The porosity of this HX (ϕ_1) is calculated to be around 54%.

The second ambient heat exchanger (AXH2) is fabricated from a circular copper block and is 2 cm long in the x direction. Gas passages are obtained by drilling 574 holes with a diameter of 2.5 mm in parallel to its axis. Cooling water passages are obtained by drilling 4 channels with a diameter of 5 mm perpendicularly to the HX axis. The water also flows partially around the perimeter of the block. The porosity of this HX (ϕ_2) is about 33%. The hydraulic radius of the pores is $R_h \approx 0.6$ mm. Compared to AHX1 this HX is characterized by a simpler fabrication technique but the circular pore geometry hardly allows for porosities to exceed 40 %.

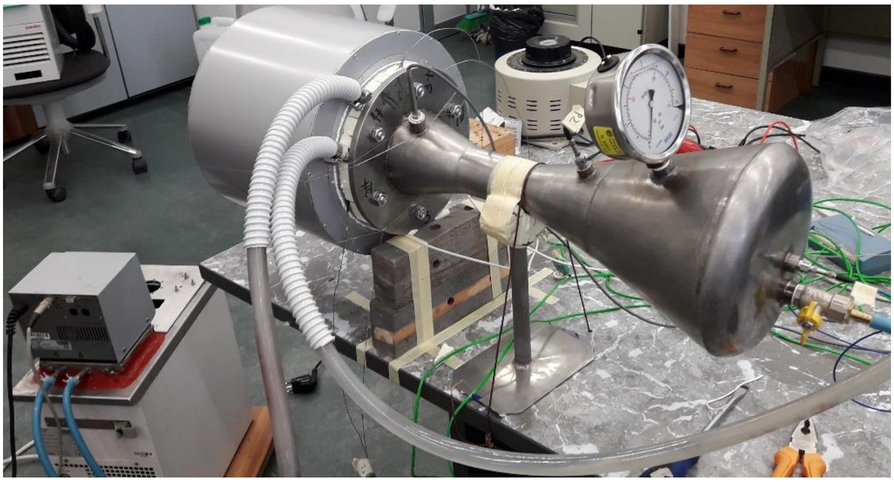

Figure 3. Photograph of the experimental apparatus.

Note that these two HXs are both made of copper, have the same length along the resonator axis (2 cm), have pores of almost equal hydraulic radius and have the same flow arrangement (cross flow with four water-tube passes). Their comparative study should therefore allow for investigating the impact of pore geometry and associated porosity on the engine performance.

At the working frequency of the engine ($f \approx 143$ Hz) the thermal penetration depth of the gas

$$\delta_\kappa = \sqrt{\frac{2\kappa}{\omega}} \tag{1}$$

(κ and ω being the gas thermal diffusivity and the angular frequency respectively) amounts approximately to $\delta_\kappa \approx 0.23$ mm so that $R_h/\delta_\kappa \approx 2.2$ for AHX1 and $R_h/\delta_\kappa \approx 2.6$ for AHX2. These values are compatible with good thermal contact conditions between the gas and the HX solid walls [4]. Spacers were used to separate the HXs from the stack by a gap of about 1.5 mm.

The standing wave engine in place for testing is shown in Fig. 3. The cylindrical sleeve seen on the left is filled with rock wool to thermally insulate the “hot” parts of the engine (the hot duct, the heater and the stack holder). A strip of a polystyrene sheet 2 cm thick has been also wrapped around the ambient HXs for thermal insulation purposes.

2.2 Measurements

For dynamic pressure measurements a microphone (Brüel and Kjær instruments, type 4938, sensitivity 1.6 mV/Pa) and two piezoelectric pressure transducers (PCB Piezotronics, model 113B28, sensitivity 14.5 mV/kPa) were flush mounted on the resonator walls. The signals recorded by these sensors (labeled as P1, P2 and P3 in Fig. 1), when combined with simulations performed using the DeltaEC code (configured for matching the P1, P2 and P3 values) make it possible to reconstruct the profile of the acoustic wave along the resonator axis and to estimate parameters of interest such as the amplitude of the dynamic pressure at a pressure antinode (P_A), the amplitude of the oscillatory velocity at the HXs location (v_1) and the flow of acoustic energy across a given section or component. A typical result is shown in Fig. 4 where the axial distributions of the magnitude of the acoustic pressure, *p*, and volumetric velocity, *U*, are reported. It can be seen how the AHX is located around midway between the velocity node and antinode of the standing wave so that a wide range of velocity amplitudes (and associated gas displacement amplitudes) can be selected by varying the heat input to the system.

To measure the average gas/solid temperature of the heater, T_H, a type-K thermocouple (error ±0.3 °C), labeled as T0 in Fig. 1, was placed inside a pore located at the centre of the heater.

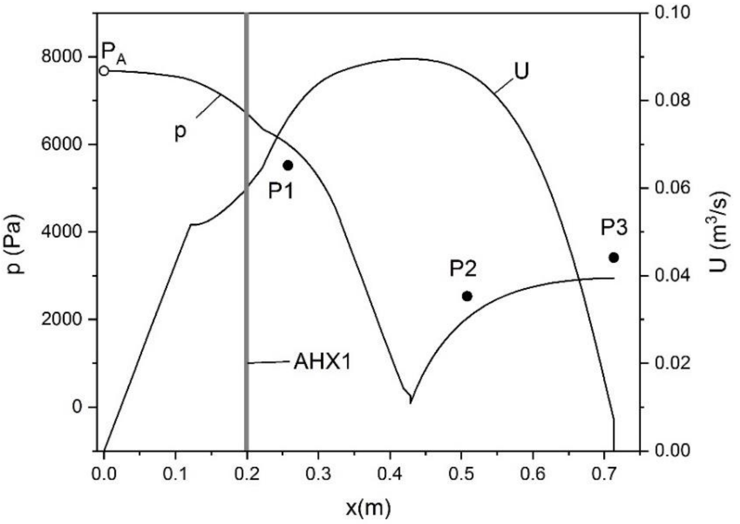

Figure 4. Axial distributions of the magnitude of the acoustic pressure, *p*, and volumetric velocity, *U*, when the heat input to the engine (integrating AHX1) is 583 W. Full circles are the pressure values measured by P1, P2 and P3. The vertical grey line indicates the AHX location.

As for AHX1, two type-K thermocouples (labeled as T1 and T2) were placed in the water tubing at the inlet and outlet sections of the HX to measure the local water temperature (T_1 and T_2 respectively). To measure the temperature T_m of the gas flowing inside a pore a thermocouple (labeled as T3) was installed through a spacer in the (slightly enlarged) gap between two fins located at the centre of the HX. To measure the temperature T_s at the base of the fins a thermocouple (labeled as T4) was glued on the flat wall of the water pipe by copper spray. A schematic of the installation of T3 and T4 can be seen in Fig.2.

As for AHX2, two type-K thermocouples (labeled as T1 and T2) were placed in the water tubing at the inlet and outlet sections of the HX to measure the local water temperature (T_1 and T_2, respectively). To measure the temperature T_m of the gas flowing inside a pore a thermocouple (labeled as T3) was inserted into a ceramic sleeve of squared cross section and the assembly was then fitted in a (slightly enlarged) pore. Since the contact area between the sleeve and the pore walls is restricted to the sleeve corners this probe reasonably measured the temperature of the gas. To measure the temperature T_s of the solid honeycomb matrix a thermocouple (labeled as T4) was imbedded in a hole drilled in the copper matrix just near T3. Copper spry was used to enhance thermal contact. The remaining two thermocouples (labeled as T5 and T6) have been analogously installed to measure T_m and T_s but in a more peripherical location compared to T3 and T4 so as to get the information on the radial distribution of the measured temperatures. A schematic of the installation of T3, T4, T5 and T6 can be seen in Fig.2.

The thermocouple signals are acquired by a 8-channel data logger connected to a PC (USB-Temp device of Measurement Computing) while the dynamic pressure sensor signals are read, after being preamplified, directly on multimeters as output voltages.

The input heat flux $\dot{Q}_H$, generated by feeding the heater through a variable voltage autotransformer, was calculated by measuring the voltage drop across the heater and the flowing current.

The heat power transferred by the AHX is measured through a closed loop water circuit. The network comprises (a) a refrigerated/heating circulator unit pumping the water and controlling its temperature, (b) a valve installed downstream the AHX regulating the water flow rate, (c) a rotameter (accuracy ± 5 l/h) installed upstream the AHX measuring the water flow rate and (d) a thermal storage system placed outdoors constituted by a copper coil immersed in a water bath. The last system was utilized because the circulator is unable to absorb thermal loads on the AHX higher than 200 W. The inlet temperature of the water is set at 25 °C in all measurements.

To avoid moisture condensation on the solid surfaces of the HXs and stack each measurement cycle started by emptying the resonator through a vacuum pump. While the vacuum pump is left in operation for at least ½ hour the heater is heated up to about 50÷60 °C and cooling water at 25 °C is sent into the AHX. Then the vacuum pump is disconnected and external air is left to enter the resonator. Finally, the engine is brought to the desired operating point and measurement is conducted after thermal equilibrium conditions are reached.

2.3 Data reduction

The AHXs' heat transfer rates are estimated from the measured inlet/outlet water temperatures and water volume flow rate, $\dot{V}$, as

$$\dot{Q}_A = \dot{V}\rho_w c_w (T_2 - T_1) \tag{2}$$

ρ_w and c_w being the density and specific heat of water respectively.

It must be observed that the measured heat flux $\dot{Q}_A$ comprises different contributions and precisely: (1) the thermo-acoustically activated hydrodynamic heat flux $\dot{Q}$ along the stack (the parameter of interest for the estimation of the gas-side heat transfer coefficient), (2) the conduction heat flux $\dot{Q}_{K1}$ transported by the gas and the solid portion of the stack, (3) the conduction heat flux $\dot{Q}_{K2}$ transported by the stack-holder walls and thermal insulating sleeve (4) the conduction heat flux $\dot{Q}_{K3}$ transported by the resonator walls over which dissipation of acoustic power occurs and finally (5) the conduction heat flux $\dot{Q}_{leak}$ due to heat leakage from the heat exchanger to the surrounding environment through the insulation. Heat balance provides the following equation

$$\dot{Q}_A = \dot{Q} + (\dot{Q}_{K1} + \dot{Q}_{K2} + \dot{Q}_{K3}) - \dot{Q}_{leak} \tag{3}$$

Therefore, to calculate $\dot{Q}$ the above conduction heat fluxes have to be estimated. To accomplish this a combination of both static measurements and simulation procedures is applied.

In the static measurements the heater was powered below the onset temperature of the engine and the thermal load on the AHX corresponding to

$$\dot{Q}_{A,static} = \dot{Q}_{K1} + \dot{Q}_{K2} - \dot{Q}_{leak} \tag{4}$$

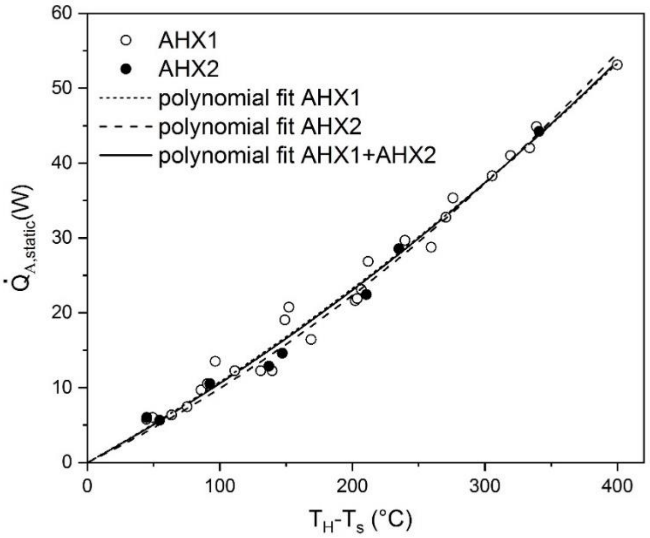

Figure 5. The conductive heat flux measured under static measurements for AHX1 (open circles) and AHX2 (full circles). Dotted, dashed and continuous lines are 2nd order polynomial fits of the experimental points concerning AHX1, AHX2 and both AHX1 and AHX2 respectively.

was measured through Eq. (2). Results are shown in Fig. 5 where $\dot{Q}_{A,static}$ is reported as a function of the temperature difference between the heater, T_H, and the AHX, T_s, for both AHX1 (open circles) and AHX2 (full circles). The least-squares fit of the two sets of experimental data by a 2nd order polynomial of the form $A_1(T_H\text{-}T_s)+A_2(T_H\text{-}T_s)^2$ is represented by the dotted (AHX1) and dashes (AHX2) lines. The relative difference between these two curves results lower than 5% according to the fact that the thermal path from the heater to the AHXs is equal in the two cases. So, for subsequent analysis the curve fit of all the experimental points (both AHX1 and AHX2) is considered. The resulting values for the fitting parameters are A_1=0.09624±0.00441 and A_2=(9.43334±1.54)×10^{-5}, the coefficient of determination being R^2=0.988. Subtracting now Eq. (4) from Eq. (3) provides

$$\dot{Q} = \dot{Q}_A - \dot{Q}_{A,static} - \dot{Q}_{K3} \tag{5}$$

The heat flux $\dot{Q}_{K3}$ to be substituted in this equation together with $\dot{Q}_{A,static}$ for the determination of $\dot{Q}$ was derived by simulating the energy fluxes in the engine using DeltaEC. The acoustic power flowing downstream the AHX toward the conical duct (on the right of the AHX in Fig. 1) is identified with $\dot{Q}_{K3}$.

Note that the above method does not require the direct determination of $\dot{Q}_{leak}$ since this term is included both in $\dot{Q}_A$ and in $\dot{Q}_{A,static}$ and it elides after Eq. (4) is subtracted from Eq. (3).

To make $\dot{Q}$ consistent with the outlet temperatures of water these last are recalculated as follows

$$T_2' = T_2 - \frac{(\dot{Q}_{A,static} + \dot{Q}_{K3})}{\rho_w c_w \dot{V}} \tag{6}$$

where T_2' represents the outlet temperature of water that would be measured if the conduction contributions were absent, i.e., if the AHX was uniquely loaded by the hydrodynamic heat flux.

The heat transfer and temperature values so determined are then used to calculate the overall heat transfer coefficient, *UA*, as [25]

$$UA = \frac{\dot{Q}}{\theta_{ml}} \tag{7}$$

where θ_{ml}, the log-mean temperature difference, has the following expression

$$\theta_{ml} = \frac{T_2' - T_1}{\ln\left(\dfrac{T_m - T_1}{T_m - T_2'}\right)} \tag{8}$$

when considering that in oscillatory flows the inlet and outlet temperatures of the primary fluid (the gas) are the same (T_m).

In the case of AHX1 the finned geometry allows the gas-side heat transfer coefficient *h* to be estimated from the *UA* values. A simplified 1D heat transfer model provides, in fact, the following expression for *UA*

$$UA = \frac{1}{\dfrac{1}{h_w S_w} + \dfrac{d}{K_t S_w} + \dfrac{1}{h\left[\sum_i (\Pi L_{fi})\eta_{fi} + S_b\right]}} \tag{9}$$

where h_w is the water-side heat transfer coefficient, S_w is the total inner surface of the water tubes, K_t is the thermal conductivity of the tube material (copper), *d* is the wall thickness of the tube, Π is the perimeter of the fin cross section, L_{fi} is half the length of the i-th fin, S_b is the total area of the unfinned external surface of the tubes and where η_{fi}, the efficiency of the i-th fin, has the following expression

$$\eta_{fi} = \frac{\tanh(mL_{fi})}{mL_{fi}} \qquad m = \sqrt{\frac{h\Pi}{A_f K_f}} \tag{10}$$

A_f and K_f being the cross-section area and thermal conductivity of the fin respectively.

In Eq. (9) the parameter h_w has to be measured beforehand. To accomplish this the AHX was set in isothermal conditions by immersing it in a water bath maintained at 50 °C. A flow $\dot{V}$ of water at 25 °C was then sent to the HX inlet section. If the temperature of the fin base T_s is assumed equal to the temperature of the internal surfaces of the water tube, standard energy balance calculations for the case of internal flow with constant surface temperature [25] provide the following expression of h_w in terms of measured quantities

$$h_w = \frac{\dot{V}\rho_w c_w}{S_w} \ln\left(\frac{T_s - T_1}{T_s - T_2}\right) \tag{11}$$

Obviously, the effectiveness of this procedure relies on the assumption of constant surface temperature that constitutes the major approximation of the method. However, using a thin tube wall (d=1 mm) and of high thermal conductivity (K_t≈400 W/mK) the approximation should be reasonable. For a water flow rate of 60 l/h, for example, the method furnished the value h_w=2496±21 W/m^{2}K (the indicated accuracy being the standard deviation of measurements).

2.4 Error analysis

To estimate the measurement uncertainty standard error propagation procedures [17] are applied. To reduce the error in the measurement of temperature differences ΔT an accurate in situ calibration of the thermocouples was performed by an environmental test chamber. This decreased the error in ΔT to ±0.2 °C. Analogously, the uncertainty in the measurement of the flow rate of water was decreased to ± 0.3 l/h after calibration of the rotameter through accurate measurements of the volume of water collected in a precision graduated cylinder in a given time. To reduce the error in the calculation of $\dot{Q}_A$ and θ_{ml} the flow rate of water was decreased gradually from 53.8 l/h at the highest heat transfer rates to 17.3 l/h at the lowest ones. This allowed for relatively large water temperature drop across the AHX (> 7 °C) maintaining, accordingly, the relative uncertainty on $\dot{Q}_A$ lower than 4.2% and that on θ_{ml} lower than 7 %. A higher relative error (~10 %) affects the measurement of the heat flux $\dot{Q}_{A,static}$ since the low conductive heat transfer rates give rise to smaller temperature differences across the AHXs (< 2.2 °C). From the above values it results that the relative error of the heat fluxes $\dot{Q}$ as calculated by Eq. (5) varies from about 4% at the highest heat transfer rates to 17 % at the lowest ones. Analogously, the relative error affecting the heat transfer coefficient h varies from about 8% to 24 %. These trends reflect the decrease in temperature differences across the AHX as the heat transfer rates are reduced. The uncertainty values of the Nusselt number are represented by error bars in Fig. 10.

3. Results and discussion

3.1 Impact of HXs on engine performance

The impact of the two HXs on the engine performance in converting heat to acoustic power can be deduced from Fig. 6 where the square of acoustic pressure amplitude measured by P1, P2 and P3 is reported as a function of the electric power input to the engine $\dot{Q}_H$ when a steady state is reached. Results show how AHX1 increases the engine performance compared to AHX2 since the acoustic pressure amplitudes measured at the selected microphone locations are higher for AHX1 than for AHX2 at every input power level.

The difference in performance cannot be fully captured from Fig 6, however, since the temperature difference across the stack, which influences the generated acoustic power, is different in the two cases as shown in Fig. 7 where (T_H-T_s) is reported as a function of $\dot{Q}_H$.

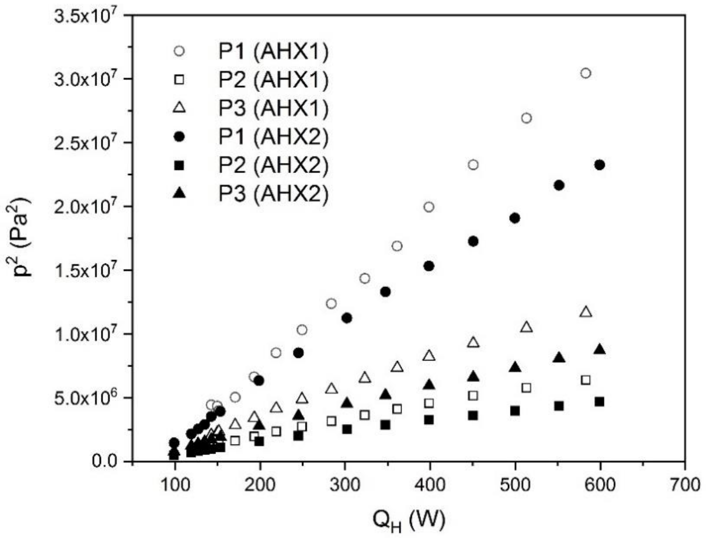

Figure 6. The square of the acoustic pressure measured by P1, P2 and P3 as a function of the heat input to the system.

So, for assessing the impact of the two HXs on the engine performance the thermal-to-acoustic conversion efficiency normalized by the Carnot efficiency is considered as a relevant indicator:

$$\frac{\eta}{\eta_C} = \frac{W_a}{\dot{Q}_H}\left(1 - \frac{T_s}{T_h}\right)^{-1} \tag{12}$$

where W_a, the acoustic power produced by the engine core (the stack/HXs assembly), is calculated by DeltaEC (configured for matching the P1, P2 and P3 values) as the sum of the acoustic energy fluxes leaving the ambient HX and the heater from the sides facing the resonator. Results are shown in Fig. 7 where η/η_c is reported as a function of $\dot{Q}_H$. The normalized efficiency of the engine integrating AHX1 is reduced on average by 27% (the efficiency by 23%) when AHX2 is installed, despite the fact that in the last case a higher temperature gradient exists in the stack.

The lower performance of AHX2 and the higher operating temperature, seems to indicate that some acoustic loss mechanisms is at play that is more pronounced in AHX2 than AHX1. Furthermore, this loss mechanism grows with the acoustic amplitude since the difference between the temperature gradients of the two HXs increases with $\dot{Q}_H$.

Although AHX2 has a smaller heat transfer area compared to AHX1 the viscous dissipation occurring on the HXs surfaces could be, at least partially, responsible of the observed behavior. For a given volumetric flow, in fact, the local velocity amplitude v_1 in AHX2 should be about $\phi_1/\phi_2 \approx 1.64$ times higher than the velocity amplitude in AHX1. So, the viscous dissipation per unit area of AHX2 should be around $(\phi_1/\phi_2)^2 \approx 3.28$ times higher than the one on AHX1. Taking into account that AHX2 has surface area $\phi_2 R_{h1}/\phi_1 R_{h2} \approx 0.61$ times smaller than AHX1 it follows that the dissipation of acoustic power on AHX2 is almost double that on AHX1.

An additional loss mechanism could be caused by the complex flow structures occurring at the HX-stack and HX-duct junctions due to the difference in porosity. The fluid motion entering and leaving the HX pores is characterized, in fact, by turbulent flow through sharp corners during fluid entrance into the pores and vortex formation and shedding during the fluid ejection from the pores [26]. These effects are likely to be less important for AHX1 whose finned geometry and higher ϕ should minimize eddy production in the acoustic flow [27]. The dissipated power, assumed of the order of $A_g \rho_m v_1^3$ [18] (where ρ_m is the mean gas density) should be around 3 times higher in AHX2 than in AHX1.

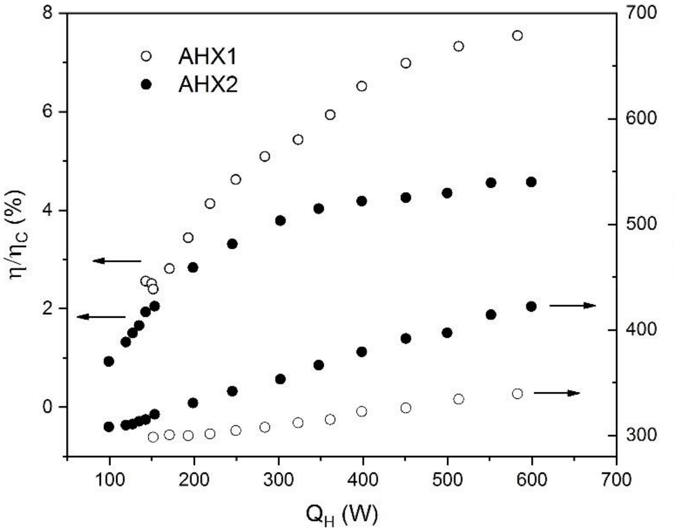

Figure 7. The normalized efficiency (on the left scale) and the temperature difference between the "hot" and "ambient" heat exchanger (on the right scale) as a function of the heat input to the system.

Although the above arguments could not fully account for the excess of the temperature difference (T_H-T_s) measured in AHX2 compared to AHX1 they illustrate that the HX pore geometry and porosity could have a non-trivial effect on flow losses, especially when the HX is located in high velocity regions of the acoustic field, as in the present investigation.

An additional explanation of the improved performance of the engine containing AHX1 is found when taking into account that a figure of merit of a HX reflects its ability to sustain high transfer rates under small gas-solid temperature differences. This favorable property, in fact, decreases the thermal irreversibility associated with the heat transfer and leads to an enhancement of the overall engine performance. The time averaged gas-solid temperature differences ΔT_{ms} ($=T_m$-T_s) measured for the two HXs are reported in Fig. 8 as a function of the drive ratio DR defined as the ratio of the pressure amplitude at the wave pressure antinode P_A (calculated by DeltaEC when configured for matching the P1, P2 and P3 values) to the mean pressure P_m.

As expected, AHX1 entails lower ΔT_{ms} values as being characterized by a lower UA factor. The last parameter, calculated by Eq. (7) for both HXs, is plotted in Fig. 9 as a function of the local peak acoustic Reynolds number

$$\mathrm{Re}_{D1} = \frac{\rho_m D_h v_1}{\mu} \qquad (13)$$

where D_h is the hydraulic diameter of the HX pore and μ the dynamic viscosity. The lower value of *UA* found for AHX2 compared to AHX1 reflects the lower heat transfer area and, presumably, the different influence of the complex flow at the HX junctions on the local heat transfer coefficient. The lower *UA* value leads to higher gas-solid temperature differences and so to higher irreversibility associated to heat transfer.

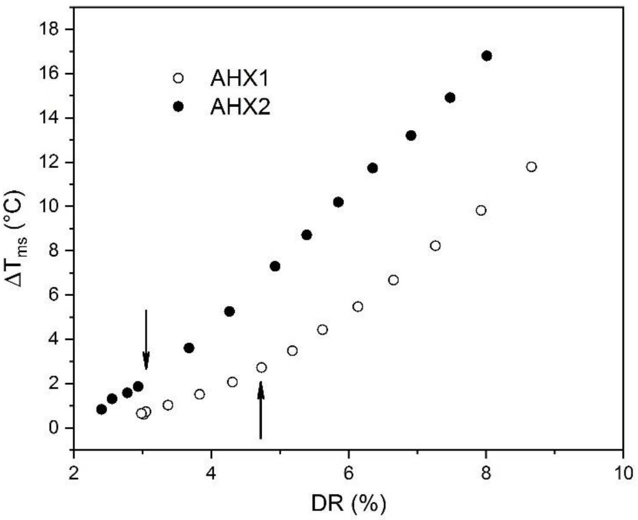

Figure 8. The gas-solid temperature difference as a function of drive ratio for both AHXs.

Vertical arrows in Fig. 8 indicate the pressure amplitude for which the peak-to-peak displacement amplitude ($2\xi_1$) equals the HX length. In both curves the growth of ΔT_{ms} with *DR* seems linear in the *DR* interval below the arrow and faster above. This result could be explained on the basis of the BLC model proposed by Swift which just predicts a linear behavior at low acoustic amplitudes and a squared-one at high acoustic amplitudes as stated by the formula

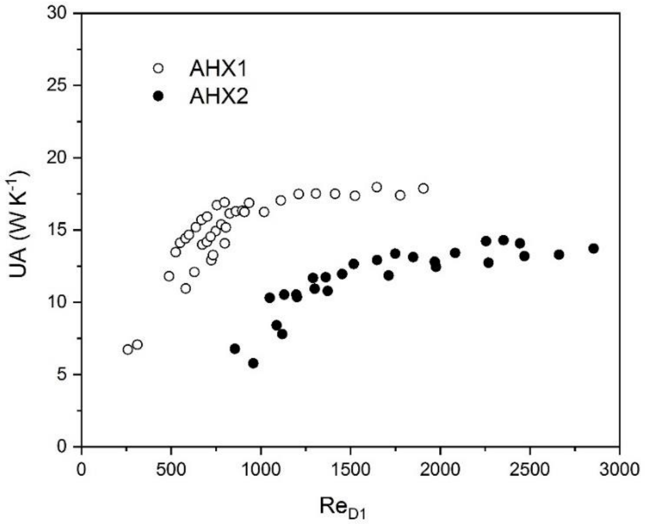

Figure 9. The UA coefficient as a function of the peak Reynolds number for both HXs.

$$\Delta T_{ms} = \frac{\dot{Q} y_{eff}}{KS} = \frac{\dot{Q} R_h}{K A_g} \frac{y_{eff}}{x_{eff}} \qquad (14)$$

where x_{eff}=min{$2\xi_1$, L_{HX}} and *S* is the actual gas-solid heat transfer area (proportional to x_{eff}). The predicted behavior takes into account that $\dot{Q} \propto P_A^2$ and that at low acoustic amplitudes (when $2\xi_1 < L_{HX}$) x_{eff} grows as $2\xi_1$ and so proportionally to P_A. This should make ΔT_{ms} to depend linearly on P_A. At high acoustic amplitudes (when $2\xi_1 > L_{HX}$) x_{eff} is constant and equal to L_{HX} and so ΔT_{ms} is expected to exhibit a quadratic dependence on P_A.

In conclusion, the analysis performed in this subsection evidences how AHX2, due to its pore geometry and lower porosity compared to AHX1, is affected by higher irreversibility, both viscous and thermal, which degrades the engine performance.

3.2 Heat transfer correlations

The gas-side heat transfer coefficient estimated as described in section 2.3 and expressed in terms of dimensionless Nusselt number

$$\mathrm{Nu}_D = \frac{hD_h}{K} \tag{15}$$

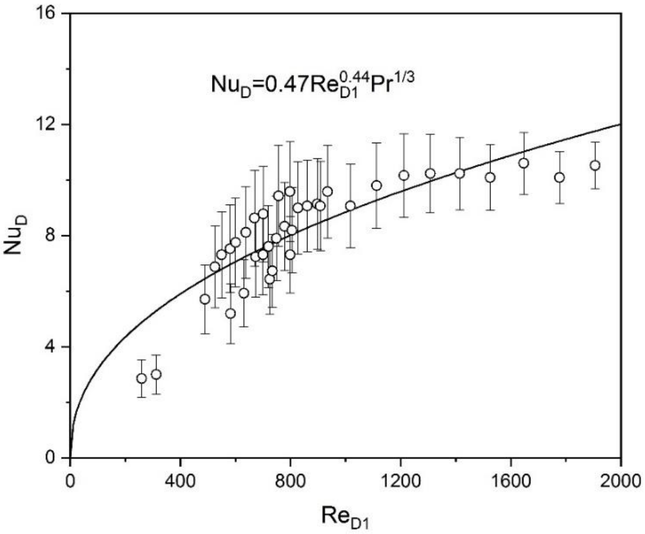

Figure 10. Measured gas-side Nusselt number as a function of acoustic Reynolds number (open circles) for AHX1 and correlation law obtained from data regression (continuous line).

(D_h being the hydraulic diameter of the HX pores) is reported in Fig. 10 as a function of $\mathrm{Re_{D1}}$ (open circles). The graph shows that as $\mathrm{Nu_D}$ increases with $\mathrm{Re_{D1}}$ it reaches a quite constant value above $\mathrm{Re_{D1}}\approx 1200$, where the gas peak-to-peak gas displacement amplitude equals the fin length. The continuous line is a least-squares fit of the experimental points by the function $\mathrm{Nu_D=aRe^bPr^{1/3}}$ with a coefficient of determination R^2=0.73. The resulting correlation law is

$$\mathrm{Nu}_D = 0.47\,\mathrm{Re}_{D1}^{0.44}\,\mathrm{Pr}^{1/3} \tag{16}$$

In Fig. 11 a comparison with the results of other experimental researches found in literature with regard to HXs of the same configuration (finned-type HXs) is reported.

Nsofor et al. [28] tested a parallel-plate HX made of copper with fin spacing of 0.95 mm and fin thickness of 0.15 mm. The HX worked as the hot HX of a TA refrigerator filled with He at mean pressures ranging from 3 to 8 bar and operation frequencies ranging from 300 to 450 Hz. The heat transfer correlation derived from measurements, after conversion of the rms Re number to peak Re number, is:

$$\mathrm{Nu}_D = 0.548\,\mathrm{Re}_{D1}^{0.31}\,\mathrm{Pr}^{0.11} \tag{17}$$

This function is plotted in Fig 11 as a dotted line.

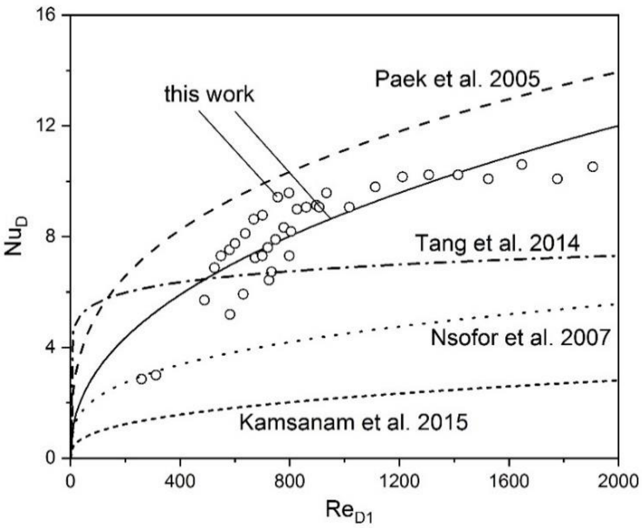

Figure 11. Comparison among the experimental data (open circles) and correlation law (continuous line) obtained in this work for the gas-side Nusselt number and correlation laws experimentally derived by other researchers for heat exchangers of the same type of AHX1.

Paek et al. [29] studied the heat transfer characteristics of finned-tubes HXs made of aluminum with fins spaced 0.54 mm apart. This HX was integrated as cold HX in a TA cooler filled with three He-Ar mixtures (44% He, 33 % He, 22 % He) at three different mean pressures (20, 13.3 and 6.7 bar) and driven near its resonance frequency (136-155.9 Hz). The heat transfer correlation derived from measurements, after conversion of Colburn-*j* factor to Nusselt number, is:

$$\mathrm{Nu}_D = 1.303\,\mathrm{Re}_{D1}^{0.3271}\,\mathrm{Pr}^{1/3} \tag{18}$$

This function is plotted in Fig 11 as a dashed line.

Tang et al. [30] built an experimental apparatus reproducing the operating conditions of pulse tube refrigerators to investigate the heat transfer performance of a finned HX made of copper and cooled by a flow of water through channels surrounding the HX. The fins were 0.75 mm thick, 20 mm long in the flow direction and spaced 0.75 mm apart. The working gas was He at three mean pressures (25, 30 and 35 bar) while the operating frequency varied in the range 40-110 Hz. The test results were summarized in terms of peak Reynold number and Valensi number (Va) as follows

$$\mathrm{Nu}_D = 0.43\,\mathrm{Re}_{D1}^{0.0876}\,\mathrm{Va}^{0.405} \tag{19}$$

where

$$\mathrm{Va} = \frac{\rho_m \omega D_h^2}{\mu} \tag{20}$$

This function (with Va=211 for the experimental conditions of the present study) is plotted in Fig. 11 as a dash-dotted line.

Kamsanam et al. [31] performed measurements of heat transfer on coupled finned-tube HXs (without stack) placed side-by-side in a resonator filled with He. Three HXs made of copper with fin thickness of 0.3 mm, fin length of 20 mm and different fin spacing (0.7, 1.4 and 2.1 mm) were investigated. The correlation obtained from regression of their data, after conversion of Colburn-*j* factor to Nusselt number, is

$$\mathrm{Nu}_D = 0.203\,\mathrm{Re}_{D1}^{0.3606}\,\mathrm{Pr}^{1/3}\left(\frac{t}{D_h}\right)^{-1.2541} \tag{21}$$

t being the fin thickness. This function is plotted in Fig. 11 as a short-dashed line.

The analysis summarized in Fig. 11 reveals that, although all reported correlations refer to the same HX configuration (i.e. a finned-type HX), they are not univocal with very marked deviations which can be as high as 400% as in the case of the correlations proposed by Paek et al. and Kansanam et al. The lower deviation (~ 32%) is found between the correlation derived in the present work and the one proposed by Paek et al [29]. This finding seems to indicate that differences in geometrical parameters (even for HX of the same configuration) and differences in operating conditions (mean pressure, frequency, working fluid, mean temperatures) may have a considerable effect on heat transfer in oscillatory flow. Hence, the definition of general correlation laws applicable to different geometrical configurations and over wide ranges of operating conditions could be an arduous task. This circumstance is well evidenced in the study of Kamsanam et al. [32] where it is found that finned-tube HXs differing uniquely by the plate spacing but working under the same operating conditions are characterized by quite different heat transfer correlation laws.

In Fig. 12 a comparison of the obtained Nusselt number with the predictions of heat transfer models currently applied in thermoacoustics is shown. The models considered here are the BLC, TASFE and RMS-Re models.

The BLC model proposed by Swift [3] and integrated in the DeltaEC code, estimates the heat transfer coefficient by the relation

$$h = \frac{K}{\min\{R_h, \delta_\kappa\}} \tag{22}$$

which is plotted in Fig. 12, after conversion into Nu_D number, as a dotted line.

In the TASFE model classical steady flow heat transfer correlations of the type Nu=Nu(Re, Pr) are converted to the case of oscillatory flows by taking their time average over an acoustic cycle. In the conversion procedure a sinusoidally oscillating velocity, $v_1\sin(\omega t)$, is assumed and substituted for the velocity appearing in the Reynolds numbers of the selected steady flow correlation. The time average over one-half cycle of the resulting time-dependent Nusselt number is then computed:

$$\mathrm{Nu}_{D,TASFE} = \frac{\omega}{\pi}\int_0^{\pi/2} \mathrm{Nu}_D(\mathrm{Re}_{D1}\sin\omega t, \mathrm{Pr})\,dt \tag{23}$$

Similarly, in the RMS-Re model the Reynolds numbers appearing in the steady flow correlation are substituted by their rms values:

$$\mathrm{Nu}_{D,RMS} = \mathrm{Nu}_D(\mathrm{Re}_{D1}/\sqrt{2}, \mathrm{Pr}) \tag{24}$$

The selection from literature of the steady flow correlations to be substituted in the above equations is based on the evidence that in the investigated acoustic Reynolds number range (Re_{D1}<2000) the flow in the HX pores should be laminar [18]. Therefore, the classical correlation for laminar (external) flow over on isothermal plate of length L (already considered by Poese and Garrett [33])

$$\mathrm{Nu}_L = 0.664\,\mathrm{Re}_L^{1/2}\,\mathrm{Pr}^{1/3} \tag{25}$$

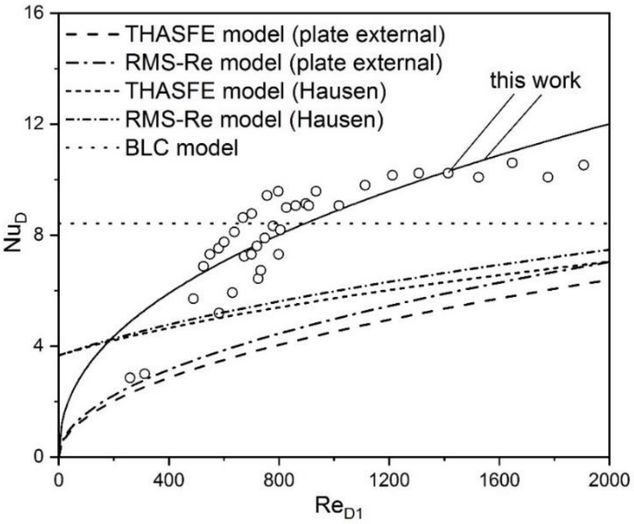

Figure 12. Comparison among the experimental data (open circles) and correlation law (continuous line) obtained in this work for the gas-side Nusselt number and correlation laws predicted by the BLC, THASFE and RMS-Re models (not continuous lines).

and the classical Hausen correlation for laminar (internal) flow in the thermal entry region (L_T) of isothermal ducts

$$\mathrm{Nu}_D = 3.66 + \frac{0.0668(D_h/L_T)\,\mathrm{Pr}\,\mathrm{Re}_D}{1+0.04[(D_h/L_T)\,\mathrm{Pr}\,\mathrm{Re}_D]^{2/3}} \tag{26}$$

are chosen.

Although Eq. (25) refers to external flow it is applied here (with $L=L_{HX}$) because the fins of the investigated HX are not tightly spaced ($R_h/\delta_\kappa \approx 4$). As for Eq. (26) its use could be justified by the fact that, as shown in experimental studies [34], the entrance length for oscillating flows inside stacks is of the order of the displacement amplitude, and so, of the HX length. Based on this evidence, when applying Eq. (26) the heat exchanger fin length has been identified with the thermal entry length ($L_{HX}=L_T$). In Fig 12 the predictions of the TASFE and RMS-Re models are plotted as dashed and dash-dotted lines respectively, as far as the eq. (25) is concerned, and as short-dashed and short-dash dotted lines respectively, as far as eq. (26) is concerned.

The plot shows how the BLC model predicts a constant Nu value, independent of Re_{D1}. The model overestimates the experimental data at Re_{D1}<600 and slightly underestimates them at

Re_{D1}>600. The mean deviation of the predicted Nu_D values from the experimental data amounts to 25%.

The TASFE and RMS-Re models predict the increase of Nu with Re_{D1} but underestimate the experimental values over almost all the investigated Re_{D1} range. The mean deviation of the Nu_D values predicted by the TASFE model from the experimental data amounts to 48% relative to Eq. (25) and to 39 % relative to Eq. (26). The mean deviation of the Nu_D values predicted by the RMS-Re model amounts to 43% relative to Eq. (25) and to 37 % relative to Eq. (26).

In summary, the results of the present study indicate that the BLC model performs better than the TASFE and RMS-Re models based on classical steady-flow correlations in predicting the heat transfer coefficients in oscillating flows. In addition, the RMS-Re modified Hausen correlation works better than the other TASFE and RMS-Re combinations investigated.

Although the BLC model reaches the best agreement with the experimental data of the present work the prediction of a constant Nu_D is in disagreement with the increase of Nu_D at low Re_{D1} values observed in this work and, generally, in all the analogous experimental investigations referred to in this section and deserve further considerations.

The dependence of Nu on Re is usually explained by observing that an increase of Re is associated to an increase of the displacement amplitude and this entails a larger number of gas particles making thermal contact with the HX [28]. This should result in an increase of both the heat exchange area and the gas-solid heat transfer coefficient.

An additional explanation could be formulated if the longitudinal distribution of heat transfer along the HX is taken into account. The BLC model assumes for HXs that the time-averaged solid temperature, gas temperature and thermal gradient along the transverse *y* direction at the gas-wall interface are constant along the whole extension of the HX (independent of *x*).

These assumption, however, doesn't agree with the results of numerical studies [7, 8, 13] which found the transverse thermal gradient, and associated heat flux density, to be dependent on the longitudinal direction *x*. Precisely, the heat flux density is observed to peak at the side of the HX facing the resonator and to change its sign near the HX-stack junction giving rise to local reverse fluxes. These reverse fluxes decrease the net heat transfer between the gas and the HXs, thus worsening the HX performance. These detriment fluxes are found to be active when $2\xi_1 < L_{HX}$. A way to suppress them is to increase the drive ratio (and associated acoustic oscillation amplitude) or, for a fixed drive ratio, to reduce L_{HX} till the condition $2\xi_1 > L_{HX}$ is met. Thus, the growth of Nu_D with Re_{D1} observed in Fig. 10 for $2\xi_1 < L_{HX}$ could simply reflect the progressive reduction of the reverse heat fluxes and the contextual improvement of the HX performance in transferring heat, which leads to higher *h* (and Nu_D) values.

5. Conclusions

In this paper an experimental investigation on the thermal performance of two TA heat exchangers characterized by a different geometry is performed. With this purpose, a test-rig, consisting of a standing wave engine was built and the HX heat transfer rates were measured over a wide range of velocity amplitudes of the oscillatory flow. The following conclusions can be drawn from the results:

– The HX with circular-pore geometry reduces the performance of the engine compared to the finned-tube HX by about 23%. Due to its circular pore geometry, lower porosity and lower global heat transfer *UA* coefficient, in fact, this heat exchanger works under higher gas-solid temperature differences, which enhances thermal irreversibility associated with heat transfer, and higher acoustic velocity amplitudes, which increases viscous losses and minor losses at the HX-stack and HX-resonator junctions. These sources of irreversibility can seriously degrade the global performance of TA engines.

– The comparison of the experimentally derived dimensionless heat transfer coefficient (Nu number) with analogous experimental works shows that correlation laws derived for different geometrical configurations and operating conditions are not univocal but very marked deviations from each other are typical. This makes the definition of general correlation laws applicable over wide configuration/operation ranges more difficult and indicates that these phenomenologically derived laws may be specific of the investigated case.

– The comparison of the experimentally derived dimensionless heat transfer coefficient (Nu number) with model predictions shows that the TASFE and/or RMS-Re models may introduce significant errors (about 40%) in the estimation of the heat transfer coefficient. The BLC model exhibits the best agreement with the experimental data, with a mean deviation of 25 %. The BLC model also accounts qualitatively for the observed dependence of the gas-solid temperature on drive ratio.

More studies (both theoretical and experimental) are needed to investigate the influence of potential reverse heat fluxes at the HX-stack junction on the growth of the heat transfer coefficient at low acoustic Reynolds number generally observed in all experimental studies.

Funding

This research was funded by the Italian Ministry of University and Research (MIUR): Project number PRIN 2017JP8PHK. The second author would like to thank EPSRC(UK) for funding under HARP2 programme (grant ref. EP/R023328/1).

References

[1] N. Rott, Thermoacoustics, Adv. Appl. Mech., 1980, 20, 135-175 and references therein.

[2] G.W. Swift, Thermoacoustic engines, J. Acoust. Soc. Am., 1988, 84 (4), 1145-1180.

[3] G.W. Swift, Analysis and performance of a large thermoacoustic engine, J. Acoust. Soc. Am., 1992, 92 (3), 1551-1563.

[4] B.L Minner., J.E. Braun, L. Mongeau, Optimizing the design of a thermoacoustic refrigerator, in: International Refrigeration and Air Conditionaing Conference, School of Mechanical Engineering, Purdue University, 1996, pp. 315e322.

[5] N. Cao, J.R. Olson, G.W. Swift, S. Chen, Energy flux density in a thermoacoustic couple, J. Acoust. Soc. Am. 1996, 99 (6), 3456-3464.

[6] H. Ishikawa, D.J. Mee, Numerical investigations of flow and energy fields near a thermoacoustic couple J. Acoust. Soc. Am. 2002, 111 (2), 831-839.

[7] A. Piccolo, Numerical computation for parallel plate thermoacoustic heat exchangers in standing wave oscillatory flow, Int. J. Heat Mass Transf. 2011, 54 (21-22), 4518-4530.

[8] E. Besnoin and O.M. Knio, Numerical study of thermoacoustic heat exchangers in the thin plate limit. Numerical Heat Transfer, Part A, 2001, 40, 445-471.

[9] E. Besnoin and O.M. Knio, Numerical study of thermoacoustic heat exchangers, Acta Acustica United with Acustica, 2004, 90, 432-444.

[10] H. Ishikawa and P.A. Hobson, Optimization of heat exchanger design in a thermoacoustic engine using a second law analysis, International Communications in Heat and Mass Transfer 1996, 23 (6) 325-334.

[11] H. Ishikawa, D.J. Mee, Numerical investigations of flow and energy fields near a thermoacoustic couple, J. Acoust. Soc. Amer. 2002, 111, 831-839.

[12] A. Piccolo, Optimization of thermoacoustic refrigerators using second law analysis, Applied Energy 2013, 103, 358-367.

[13] D. Marx and P. Blanc-Benon, Numerical Simulation of Stack–Heat Exchangers Coupling in a Thermoacoustic Refrigerator, AIAA Journal, 2004, 42, 1338-1347.

[14] M.E.H. Tijani, J.C.H. Zeegers, A.T.A.M. De Waele, Design of thermoacoustic refrigerators, *Cryogenics*, 2002, 42, 49-57.

[15] Z. Yu, A.J. Jaworski, S. Backhaus, Travelling-wave thermoacoustic electricity generator using an ultra-compliant alternator for utilization of low-grade thermal energy, Applied Energy 2012, 99, 135-145.

[16] J.P. Clark, W.C. Ward, G.W. Swift, Design environment for low-amplitude thermoacoustic energy conversion (DeltaEC), *Journal of the Acoustical Society of America* 2007, 122 (5), 3014.

[17] G. Mozurkewich, Heat transfer from transverse tubes adjacent to a thermoacoustic stack, Journal of the Acoustical Society of America 2001, 110 (2) 841-847.

[18] G.W. Swift Thermoacoustics: a unifying perspective for some engines and refrigerators, Acoust Soc Am 2002.

[19] I. Peak, J.E. Braun, L. Mongeau, Characterizing heat transfer coefficients for heat exchangers in standing wave thermoacoustic coolers. *Journal of the Acoustical Society of America*, 2005, 118, 2271-2280.

[20] J.R. Brewster, R. Raspet, H.E. Bass, Temperature discontinuities between elements of thermoacoustic devices, J. Acoust. Soc. Am. 1997, 102 (6), 3355-3360.

[21] E.C. Nsofor, S. Celik, X. Wang, Experimental study on the heat transfer at the heat exchanger of the thermoacoustic refrigerating system, Appl. Therm. Eng. 2007, 27 (14-15) 2435-2442.

[22] A.J. Jaworski, A. Piccolo, Heat transfer processes in parallel-plate heat exchangers of thermoacoustic devices–numerical and experimental approaches, *Applied Thermal Engineering*, 2012, 42, 145-153.

[23] K. Tang, Yu J., T. Jin, Y.P. Wang, W.T. Tang, Z.H. Gan, Heat transfer of laminar oscillating flow in finned heat exchanger of pulse tube refrigerator, Int. J. Heat Mass Transf. 2014, 70, 811-818.

[24] W. Kamsanam, X. Mao, A.J. Jaworski, Development of experimental techniques for measurement of heat transfer rates in heat exchangers in oscillatory flows, Experimental Thermal and Fluid Science 2015, 62, 202-215.

[25] F.P. Incoprera, D.P. De Witt, 1996, Fundamentals of Heat and Mass Transfer, third ed., Wiley and Sons, New York.

[26] L. Shi, Z. Yu, A.J. Jaworski, Vortex shedding flow patterns and their transitions in oscillatory flows past parallel-plate thermoacoustic stacks, Experimental Thermal and Fluid Science 2010 (34) 954-965

[27] K.I. Matveev, G.W. Swift, S. Backhaus, Temperatures near the interface between an ideal heat exchanger and a thermal buffer tube or pulse tube, International Journal of Heat and Mass Transfer 2006 (49) 868-878

[28] E.C. Nsofor, S. Celik, X. Wang, Experimental study on the heat transfer at the heat exchanger of the thermoacoustic refrigerating system, Appl. Therm. Eng. 2007 (27) (14-15) 2435-2442.

[29] I. Paek, J.E. Braun, L. Mongeau, Characterizing heat transfer coefficients for heat exchangers in standing wave thermoacoustic coolers, J. Acoust. Soc. Am. 2005 (118) (4) 2271-2280.

[30] K. Tang, J. Yu, T. Jin, Y.P. Wang, W.T. Tang, Z.H. Gan, Heat transfer of laminar oscillating flow in finned heat exchanger of pulse tube refrigerator, Int. J. Heat Mass Transf. 2014 (70) 811-818.

[31] W. Kamsanam, X. Mao, A.J. Jaworski, Development of experimental techniques for measurement of heat transfer rates in heat exchangers in oscillatory flows, Exp. Therm Fluid Sci. 2015 (62) 202-215.

[32] W. Kamsanam, X. Mao, A.J. Jaworski, Thermal performance of finned-tube heat exchangers in oscillatory flow conditions. International Journal of Thermal Sciences 2016 (101) 169-180.

[33] M.E. Poese, S.L. Garrett, Performance measurements of a thermoacoustic refrigerator driven at high amplitudes. Journal of the Acoustical Society of America 2000 (107) (5) 2480-2486.

[34] A.J. Jaworski, X. Mao, X. Mao, Z. Yu, Entrance effects in the channels of the parallel plate stack in oscillatory flow conditions, Experimental Thermal and Fluid Science 2009 (33) 495-502.